

1 **NO_x Emissions Constraints from GEMS NO₂ Retrievals: Inversion** 2 **Methodology and Air Quality Model Evaluation in Bangkok using** 3 **ASIA-AQ Multi-Platform Observations**

4
5 Julianna A. Christopoulos¹, Pablo E. Saide^{1,2}, Manas R. Mohanty¹, Nattamon Maneenoi¹, Jhoon Kim³,
6 Laura Judd⁴, Katherine R. Travis⁴, Savitri Garivait^{5,6}, Agapol Junpen^{5,6}, Kazuyuki Miyazaki⁷, Jinkyul
7 Choi⁷, Takashi Sekiya⁸, David Peterson⁹, Theodore M. McHardy⁹, Nicholas Gapp¹⁰, Jason M. St.
8 Clair^{11,12}, Erin Delaria^{13,14}, Glenn M. Wolfe¹¹, Abby Sebol¹⁴, Alessandro Franchin¹⁵, Changmin Cho¹⁵,
9 Morgan L. Silverman^{4,16}, James H. Crawford⁴

10
11 ¹Department of Atmospheric and Oceanic Sciences, University of California, Los Angeles, CA, USA

12 ²Institute of the Environment and Sustainability, University of California, Los Angeles, CA, USA

13 ³Department of Atmospheric Sciences, Yonsei University, Seoul, South Korea

14 ⁴NASA Langley Research Center, Hampton, VA, USA

15 ⁵The Joint Graduate School of Energy and Environment, King Mongkut's University of Technology, Thonburi, Thailand

16 ⁶Center of Excellence on Energy Technology and Environment, PERDO, Ministry of Higher Education, Science, Research
17 and Innovation, Bangkok, Thailand

18 ⁷Jet Propulsion Laboratory, California Institute of Technology, Pasadena, CA, USA

19 ⁸Japan Agency for Marine-Earth Science and Technology, Yokohama, Japan

20 ⁹U.S. Naval Research Laboratory, Monterey, CA, USA

21 ¹⁰Science Applications International Corporation, Monterey, CA

22 ¹¹Atmospheric Chemistry and Dynamics Laboratory, NASA Goddard Space Flight Center, Greenbelt, USA

23 ¹²GESTAR II, University of Maryland Baltimore County, Baltimore, USA

24 ¹³ESSIC, University of Maryland, College Park, postal code, USA

25 ¹⁴Department of Atmospheric and Oceanic Science, University of Maryland, College Park, USA

26 ¹⁵Atmospheric Chemistry Observations and Modeling Laboratory, NSF National Center for Atmospheric Research, Boulder,
27 CO, USA

28 ¹⁶Science Systems and Applications, Inc. Hampton, VA, USA

29
30 *Correspondence to:* Julianna A. Christopoulos (juliechristo@g.ucla.edu)



37
38 **Abstract.** Nitrogen Dioxide (NO_2) is a key component of tropospheric chemistry and air quality, yet large uncertainties persist
39 in regional NO_x emissions across rapidly developing megacities in Southeast Asia. Observations from the Geostationary
40 Emissions Monitoring Spectrometer (GEMS) provide new constraints on anthropogenic NO_2 variability, while the 2024 NASA
41 Airborne and Satellite Investigation of Asian Air Quality (ASIA-AQ) campaign, offers an extensive, independent dataset for
42 model evaluation. Here, we examine air quality in Bangkok using coarse (20 km) and high-resolution (4 km) WRF-Chem
43 simulations during ASIA-AQ. We develop a top-down framework that uses hourly GEMS NO_2 columns to derive constraints
44 on the daytime cycle of NO_x emissions. Emissions are first estimated from GEMS using a Cross-Sectional Flux (CSF) inversion
45 and then incorporated into WRF-Chem through a novel optimization that reshapes the magnitude and daytime structure of
46 NO_x while accounting for lifetime and satellite vertical sensitivity. GEMS-constrained NO_x emissions for March 2024 are
47 estimated at $2.7 \text{ kT month}^{-1}$ over Bangkok, approximately 75% lower than EDGAR v5. Re-running WRF-Chem with the
48 updated emissions leads to substantial improvements in modeled NO_2 magnitude and temporal variability when evaluated
49 against independent ground-based, Pandora, and airborne measurements. Remaining negative biases are consistent with a
50 systematic low bias in the GEMS v3 NO_2 product that cannot be diagnosed using satellite data alone, highlighting the
51 importance of multi-platform evaluation. Together, these results demonstrate the value of hourly geostationary observations
52 combined with high-resolution modeling as a scalable pathway for improving urban NO_x emissions estimates and air quality
53 simulations in Southeast Asia.

54 1 Introduction

55 The troposphere contains a variety of pollutants and aerosols that degrade air quality and affect human health (Chen and Chen,
56 2021; Fuller et al., 2022; Shetty et al., 2023). Nitrogen oxides ($\text{NO}_x = \text{NO} + \text{NO}_2$) are primary pollutants with significant
57 variability in space and time (Seinfeld and Pandis, 2016). Information on NO_x sources is crucial in defining its concentration
58 and distribution (Miyazaki et al., 2019). Nitrogen dioxide (NO_2) is fundamental to air quality and atmospheric chemistry, as it
59 is the primary precursor to surface ozone (O_3) and nitrate aerosols (Pörtner et al., 2022) and is independently linked to the
60 development of pediatric asthma (Anenberg et al., 2022). It is thus inherent that NO_2 , and its sources, are well quantified and
61 studied to gain insights into its environmental impact.

62
63 Over the past two decades, satellite observations of tropospheric NO_2 have revealed substantial regional variability in
64 emissions, particularly over industrial and urban areas (Goldberg et al., 2024; Park et al., 2025; Rey-Pommier et al., 2025).
65 While strict air quality policies in North America and Europe have resulted in significant NO_2 reductions, many developing
66 regions, especially the megacities of Southeast Asia, have seen increases (Elguindi et al., 2020; Georgoulis et al., 2019;
67 Miyazaki et al., 2017; Park et al., 2025; Sicard et al., 2023). Thailand, for example, has undergone rapid industrialization,
68 urbanization, and economic growth over the past 30 years, with most of this development occurring in the Bangkok



69 Metropolitan Region (BMR) (Thailand Office of the National Economic and Social Development Board, World Bank, 2017)
70 (Uttamang et al., 2018). This has led to increased emissions from vehicular traffic and industrial activity, resulting in a
71 sustained degradation of air quality (Uttamang et al., 2018). Since the mid 1990s, the BMR has frequently exceeded Thailand's
72 National Ambient Air Quality Standards (NAAQS) for particulate matter (PM) ($25 \mu\text{g m}^{-3}$) and O_3 (100 ppb), particularly
73 during the dry season (February-May) (Kumar et al., 2012; Uttamang et al., 2018, 2020, 2023). Within the BMR, there have
74 been initiatives to reduce health impacts and exposure related to $\text{PM}_{2.5}$. For example, the National Agenda Action Plan on
75 "Solving the Pollution Problems of Particulate Matter" motivated implementation measures in transport, industry, and waste
76 sectors (Aung et al., 2025). However, achieving the air quality standard has remained an issue. Modeling studies have shown
77 that O_3 levels typically peak between January and March, coinciding with increased solar radiation, higher temperatures,
78 elevated humidity, and prevailing northeasterly winds during the Northeast monsoon season. These meteorological conditions,
79 combined with rising emissions, often contribute to O_3 pollution episodes in the region (Uttamang et al., 2020). A key limitation
80 of these air quality modeling studies is the uncertainty in bottom-up anthropogenic emissions inventories, which remain a
81 significant source of error. In the BMR, uncertainties in regional emissions can be as large as a factor of 2 or higher (Bond et
82 al., 2004, 2007; Smith et al., 2011; Uttamang et al., 2020). These emissions uncertainties limit our ability to accurately simulate
83 pollutant concentrations and assess the effectiveness of emission control strategies. Thus, to address this issue, new
84 observational capabilities that can directly capture emission variability at fine spatial ($< 10 \text{ km}$) and temporal (hourly) scales
85 are needed.

86

87 We are currently entering a new era of satellite atmospheric composition monitoring with the launch of three geostationary
88 (GEO) imaging spectrometers covering a large component of the Northern Hemisphere. The Geostationary Environmental
89 Monitoring Spectrometer, GEMS (Kim et al., 2020), Tropospheric Emissions: Monitoring of Pollution, TEMPO (Zoogman et
90 al., 2017), and Sentinel-4 (Gulde et al., 2017), now provide unprecedented spatial and temporal resolution of atmospheric
91 constituents. These instruments offer hourly observations that resolve daytime variability of key pollutants, including NO_2 .
92 Until now, most studies of top-down NO_x emissions have relied on once-daily measurements from low Earth orbit (LEO)
93 satellites (i.e., OMI, TROPOMI) requiring assumptions about diurnal emission and chemistry patterns that introduce
94 uncertainties when coupled with chemical transport models, particularly those arising from coarse spatial resolution ($> 20 \text{ km}$),
95 emissions inventories, and chemical mechanisms (Park et al., 2025). Although these measurements have been invaluable for
96 global and long-term NO_x assessments, they cannot fully capture the pronounced sub-daily variability in NO_2 driven by
97 emissions, chemistry, and transport. GEO satellites now provide the capability to directly observe this hourly variability (Park
98 et al., 2025). For example, using 12 km WRF-Chem simulations Hsu et al. (2026) showed that TEMPO-derived top-down NO_x
99 emissions are broadly consistent with TROPOMI and bottom-up inventories, but noted coarse model resolution (e.g., 12 km)
100 can limit the representation of coastal meteorology and chemical nonlinearity.

101



102 GEMS was the first UV-visible hyper-spectrometer in geostationary orbit and was launched on GEO-KOMPSAT-2B on
103 February 18, 2020. GEMS measurements allow the observation of air quality constituents (e.g., NO₂, SO₂, O₃, HCHO,
104 CHOCHO, and aerosols) at a spatial resolution of 3.5 x 7.7 km² at the center of its field of regard and was the first space-based
105 instrument to provide hourly observations of these species. The GEMS field of regard covers 20 countries in Asia, E-W from
106 Japan to India, and N-S from Mongolia to Indonesia (Kim et al., 2020; Park et al., 2025). Recent work has demonstrated the
107 potential of GEMS and air quality models to estimate top-down NO_x emissions over major Asian cities during the summertime
108 (de Foy and Schauer, 2022; Park et al., 2024, 2025). These studies highlight the need for comprehensive validation involving
109 independent observations. The Airborne and Satellite Investigation of Asian Air Quality, ASIA-AQ, has provided an excellent
110 opportunity to conduct extensive validation of air pollutants across multiple Asian megacities, including Bangkok (ASIA-AQ
111 White Paper | ASIA-AQ, 2025).

112

113 In this manuscript, we aim to address these gaps specifically near Bangkok, Thailand by deriving emissions and examining
114 fine- (4 km) and coarse- (20 km) resolution Weather Research and Forecasting model coupled with Chemistry (WRF-Chem)
115 simulations driven by them during mid-March 2024. First, we derive daytime hourly NO_x emissions from GEMS over the
116 BMR in March 2024. Next, we use the GEMS emissions to constrain hourly model emissions through a novel optimization
117 technique. To conclude, we assess model performance using GEMS and independently with ground-monitor information,
118 Pandora site measurements, and airborne measurements collected during the ASIA-AQ campaign.

119

120 **2 Model configuration and experimental design**

121 To simulate air quality over the BMR, we use a regional simulation of WRF-Chem v4.2.2 in a research configuration (Table
122 1; Fig. 1)(Agarwal et al., 2024; Anav et al., 2024; Gao and Zhou, 2024; Skamarock et al., 2019). The model setup follows
123 previous WRF-Chem implementations in the Korea-United States Air Quality field study (KORUS-AQ) for air quality studies
124 over the Seoul Metropolitan Area (Choi et al., 2020; Goldberg et al., 2019; Lennartson et al., 2018; Park et al., 2021; Saide et
125 al., 2020). The model was driven by reanalysis meteorology, Final Operational Global Analysis data (FNL), and Copernicus
126 Modeling Service (CAMS) chemical boundary conditions (Commerce, 2000; Inness et al., 2019). A two-domain approach
127 with one-way nesting was incorporated to gauge strengths between coarse- and high- resolution simulations. D01 (20 km)
128 spans a large portion of the GEMS field of regard, covering primary transboundary pollution sources (e.g., deserts in
129 China/India, anthropogenic emissions from China/India). A nested 4 km domain (D02) is centered over Bangkok (Fig. 1).

130

131 Original anthropogenic emissions of trace gases and primary aerosols were based on the Emissions Database for Global
132 Atmospheric Research (EDGAR v5) (Crippa et al., 2020) inventory at 0.1° x 0.1° horizontal resolution. For D02, EDGAR
133 emissions for the transport and industrial sectors were downscaled using the Open-source Data Inventory for Anthropogenic

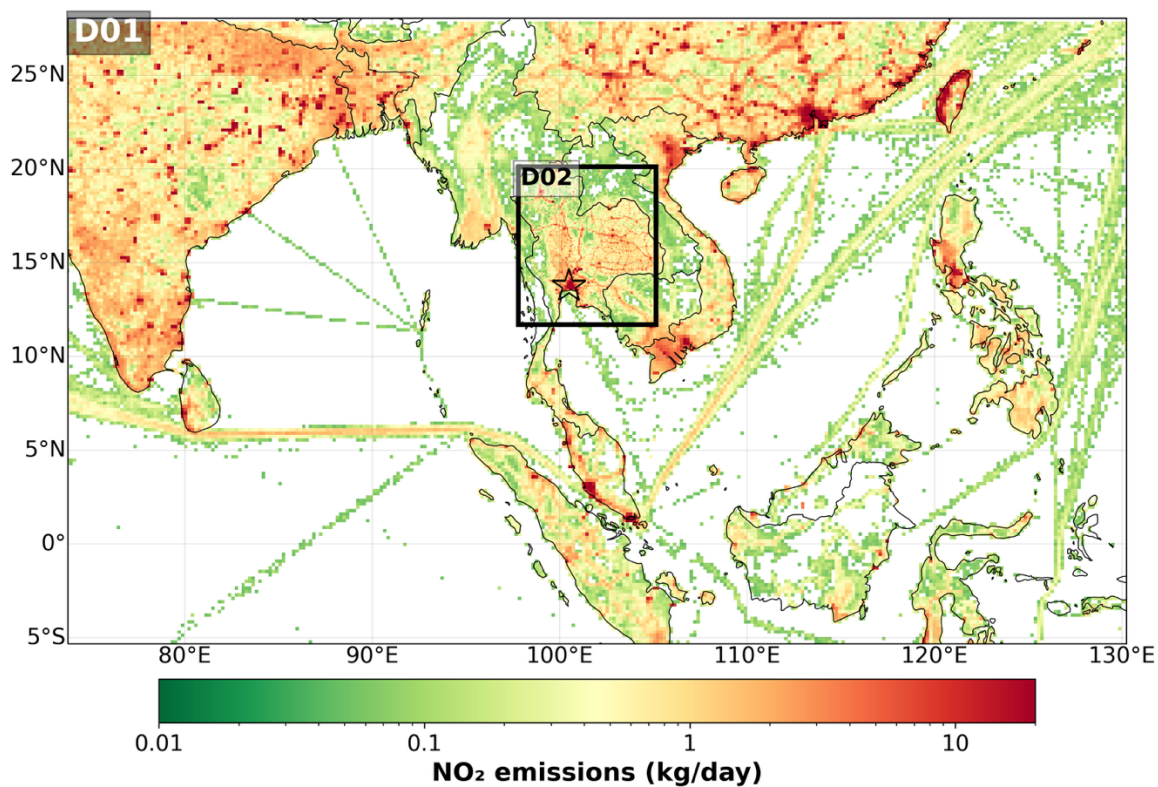


134 Carbon Dioxide emission inventory (ODIAC) at 1 km² resolution (Oda et al., 2018). This is done by distributing EDGAR
 135 emissions into the 1 km² grid using ODIAC CO₂ as a spatial proxy in a mass conserving way. Biogenic, dust, sea salt, and fire
 136 emissions were computed within WRF-Chem using the model's full-chemistry emission modules (Table 1). In this
 137 configuration, dust and sea-salt emissions are calculated every chemistry timestep, while biogenic emissions (MEGAN) are
 138 updated every 30 minutes. For fire emissions, plume rise is enabled, in which the injection heights are diagnosed using the
 139 plume-rise parameterization and emissions are vertically distributed (typically ~80% at the surface with the remainder aloft).
 140 The model was configured using the RACM-MADE-VBS (Ahmadov et al., 2012; Tuccella et al., 2015) chemical mechanism
 141 and physics parameterizations selected based on prior campaign experience (e.g., KORUS-AQ), with updates to better
 142 represent secondary organic aerosol formation, heterogenous chemistry, and aerosol properties. The modal aerosol scheme in
 143 MADE-VBS tracks both particle mass and number, allowing mode diameters to evolve dynamically with aerosol aging and
 144 growth processes. Hereafter, we will refer to this model configuration as WRF_{Base}. The model with updated anthropogenic
 145 NO_x emissions (later introduced) will be referred to as WRF_{Updated}.

146
 147 **Table 1** WRF-Chem base (WRF_{Base}) model configuration and input datasets.
 148

Component	Configuration/Source
Model Version	WRF-Chem v4.2.2
Domain	D01: 20 km (regional); D02: 4 km (nested)
Meteorological IC/BC	NCEP FNL reanalysis (1° x 1°; 6-hourly)
Chemical IC/BC	CAMS global model output
Chemistry Mechanism	RACM-MADE-VBS (with aqueous reactions)
Anthropogenic Emissions	EDGAR v5; downscaled with ODIAC CO ₂
Biogenic Emissions	MEGAN v2.1 (Guenther et al., 2006)
Biomass Burning Emissions	QFED v2.6 (Grell et al., 2011; Koster et al., 2015)
Dust Emissions	GOCART scheme (Zhao et al., 2010)
Sea Salt Emissions	Gong et al. (1997) parameterization (Gong et al., 1997)
Radiation Scheme	RRTMG (longwave); Goddard (shortwave)
Cumulus Parameterization	Grell-Freitas (D01 only)
Microphysics	Morrison (double-moment) (Ye et al., 2021)
PBL Scheme	Mellor-Yamada-Janjic TKE scheme
Simulation Period	14 – 27 March 2024

149



150

151 **Figure 1.** Spatial illustration of the WRF-Chem model domain configuration, including D01 (20 km) and D02 (4 km), and
152 average base-model NO₂ input emissions from EDGAR v5. D02 is centered over Thailand, and the urban signal associated
153 with the Bangkok Metropolitan Region (BMR) is highlighted by the star.

154

155

156

157

158

159

160

161

162

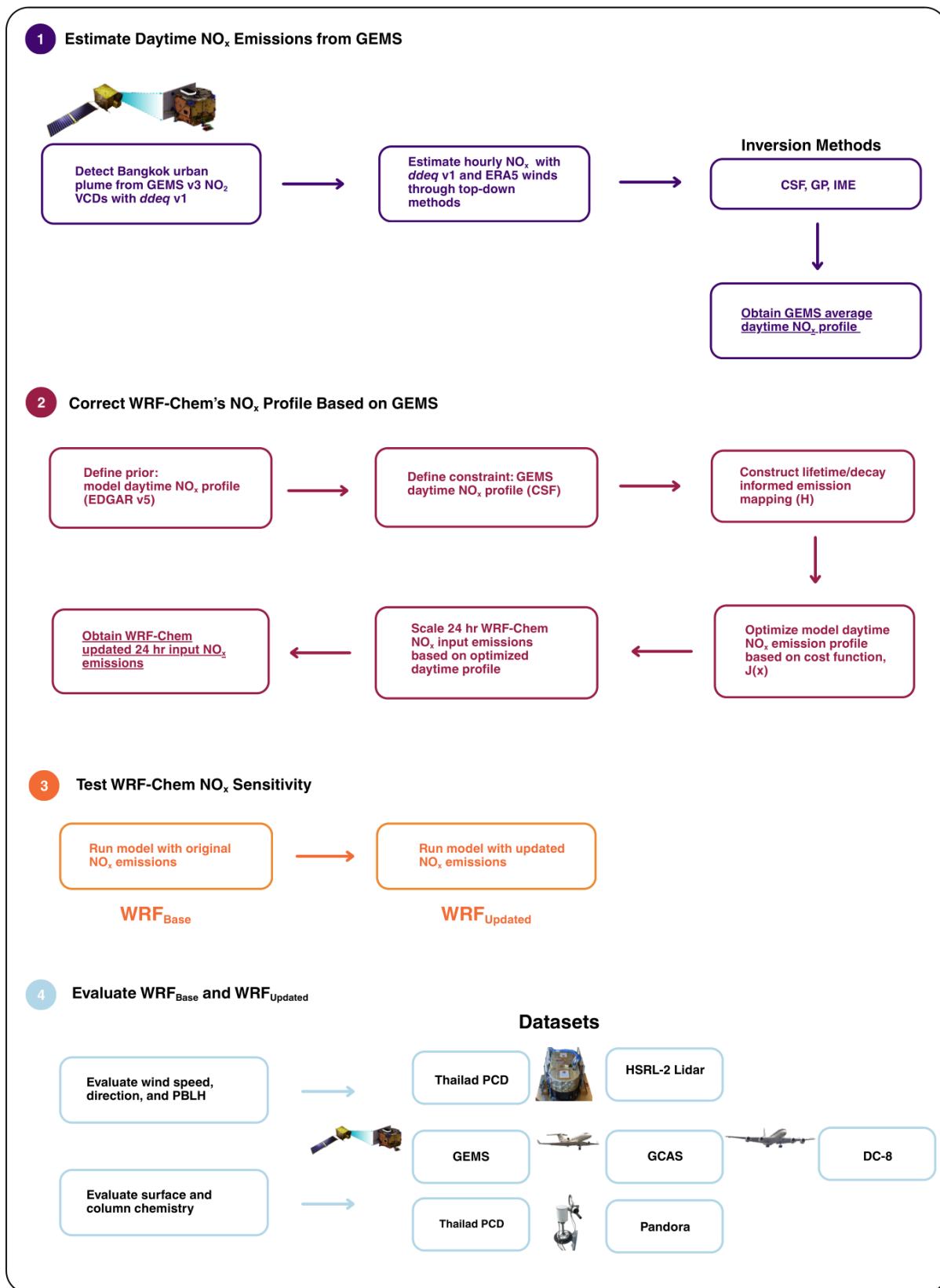
163

164

165



166
167
168
169
170
171
172
173
174
175
176
177
178
179
180
181
182
183
184
185
186
187
188
189
190
191
192
193
194
195
196
197
198
199





200 **Figure 2.** Schematic overview of the workflow used to derive satellite-constrained daytime NO_x emission profiles and assess
201 their impact in WRF-Chem over the BMR. (1) Urban NO_2 plumes are detected using GEMS tropospheric NO_2 columns, and
202 hourly NO_x emissions are estimated using top-down methods implemented in the *ddeq* v1 Python library. (2) a GEMS-derived
203 daytime NO_x profile is used to constrain the prior emission profile through an optimization framework, yielding updated input
204 24 h NO_x emissions for WRF-Chem. (3) Model simulations are performed using both the original and updated emissions. (4)
205 Model performance is evaluated against surface, column, airborne, and observations.

206 3 Satellite-derived top-down NO_x emission estimates

207 Previous studies have used satellite data (OMI, TROPOMI, SCIAMACHY, GOME (-2), OMPS) to estimate top-down NO_x
208 emissions over urban areas, but were limited to once-a-day, mid-afternoon measurements, leaving temporal variability in
209 emissions largely unaddressed (Beirle et al., 2011; Goldberg et al., 2017, 2019). Ground-based and aircraft measurements of
210 emissions can be challenging to constrain given boundary layer dynamics, such as changes in boundary layer height, stability,
211 and vertical mixing, which can strongly influence observed concentrations of trace gases (Goldberg et al., 2017, 2019).
212 Additionally, temporal allocation in bottom-up emission inventories remain a significant uncertainty, particularly at hourly
213 and daily timescales because default temporal profiles (diurnal, weekly, seasonal) often fail to capture real activity patterns,
214 meteorological influences, and sector-specific variability (Goldberg et al., 2017, 2019; Mues et al., 2014). GEMS observations,
215 however, offer a unique opportunity to provide hourly emissions rates over Bangkok, complementing existing inventories that
216 are usually provided at monthly scales. To estimate NO_x emissions over Bangkok in March 2024, we apply the methodology
217 of Kuhlmann et al. (2024), implemented through the openly available data-driven emission quantification (*ddeq* v1) Python
218 library (see step 1 Fig. 2). The standard *ddeq* library implements computationally inexpensive methods (e.g., Gaussian Plume
219 Inversion (GP), Cross-Sectional Flux (CSF) method, Integrated Mass Enhancement (IME) method) to estimate emissions from
220 Sentinel5P-TROPOMI images (Graziosi and Manca, 2025; Meier et al., 2024). One study found limited temporal sampling
221 from polar-orbiting satellites (i.e., TROPOMI) can lead to systematic underestimation of NO_x emissions, particularly because
222 wintertime conditions with higher emissions are often poorly observed due to cloud cover (Meier et al., 2024). Geostationary
223 observations, including GEMS, address this limitation by providing hourly measurements that increase the likelihood of usable
224 data on partially cloudy days and enable direct resolution of daytime emission variability, which is not accessible from once-
225 daily LEO observations. For our application, we estimate emissions for daylight hours from GEMS tropospheric column NO_2
226 data over Bangkok during the ASIA-AQ campaign. A brief description of inversion methods and specifics is provided here. A
227 complete description of the inversion methods and algorithm can be found in Kuhlmann et al. (2014).

228
229 First, within the *ddeq* framework, the source location (Bangkok; 13.7563°N, 100.5018°E), GEMS v3 NO_2 column data, and
230 ERA5 wind fields are read. We chose to incorporate ERA5 wind fields as opposed to those provided by our high resolution
231 WRF-Chem simulation in this analysis given they presented significantly lower bias when compared to surface observations



232 (Sect. 6.1). The ERA5 wind fields were downloaded and prepared by the *ddeq* library. Cloudy pixels ($CF > 0.3$) were removed.
233 Next, a plume detection algorithm is implemented to identify the Bangkok urban plume within the GEMS image. The Bangkok
234 plume subregion is estimated based on the source location and ERA5 wind field. Generally, a wind vector is taken at the source
235 location, and the plume is assumed to be located downwind, and a rectangular polygon can be drawn with the along- and
236 across- wind direction (Kuhlmann et al., 2024). An example of these plume detections and associated rectangular polygons is
237 shown in Fig. S1. To aid the algorithm's plume detection process, we identify two additional sources north of Bangkok in the
238 Saraburi province to avoid overlapping plumes from other NO_x sources. These correspond to the Khao Wong (14.692856°N ,
239 100.817204°E), and Thap Kwang (14.645313°N , 101.077650°E) regions, which we identified through NO_2 patterns visible in
240 the GEMS data in Fig. S1. These areas are not representative of Bangkok urban emissions as they are a source of industrial
241 activity related to limestone quarries and mining operations outside the inversion domain (Makkwao and Prueksasit, 2021).
242 Next, a center curve is fitted to the data and natural coordinates are calculated for the detected plume associated to Bangkok
243 to prep for the inversion algorithm. The coordinates are computed as the distance along and perpendicular to the wind vector
244 and for curved plumes this distance is computed as the arc length. Lastly, the data is prepared for the emissions estimation by
245 calculating and removing the background field and converting the NO_2 columns to kg m^{-2} . We estimate NO_x emissions using
246 three inversion techniques included in *ddeq*: CSF, GP, and IME methods. Below is a summary of the CSF method defined in
247 Kuhlmann et al. (2024). GP and IME method descriptions are available in the Supplement (e.g., S1) and Kuhlmann et al.
248 (2024).

250 3.1 Cross-Sectional Flux (CSF) framework

251 The CSF approach applies mass conservation to quantify the NO_x flux transported downwind of Bangkok using (i) the wind
252 speed perpendicular to the plume and (ii) the NO_2 enhancement integrated along the plume (line density). The NO_x flux, F (kg
253 s^{-1}), is defined as:

$$254 F = u \cdot q \quad (1)$$

255 where u (m s^{-1}) is the effective transport wind speed and q (kg m^{-1}) is the NO_2 line density. The emission rate, Q (kg s^{-1}), is
256 then inferred by correcting for chemical decay along the plume using:

$$257 Q = \frac{F(x)}{D(x,\tau)} \quad (2)$$

258 Here, $D(x, \tau)$ represents the along-plume decay for lifetime τ . Here, τ represents an effective plume lifetime that accounts for
259 both chemical decay and plume dispersion (Kuhlmann et al., 2024).

260



261 3.1.1. Effective wind speed estimation

262 The *ddeq* algorithm computes an effective wind speed, i.e., the plume-transport wind, that supports an unbiased emission
263 estimate. Ideally, this is a NO₂-enhancement-weighted average of the along-plume wind:

$$264 \quad u(x, y) = \frac{\int_0^{z_T} \rho_e(x, y, z) u(x, y, z) dz}{\int_0^{z_T} \rho_e(x, y, z) dz} \quad (3)$$

265 Here, $\rho_e(x, y, z)$ is the NO₂ enhancement, $u(x, y, z)$ is the along-plume wind speed and z_T is the plume-top height. Because
266 ρ_e is not directly observed, *ddeq* follows the approximation of Fioletov et al. (2015), in which the effective wind speed is
267 estimated using the mean of the lowest three ERA5 layers, representing the typical transport level for near-surface urban
268 plumes.

270 3.1.2. NO₂ line density calculation

271 The line density $q(x)$, is the integral of the NO₂ enhancement across the plume cross-section:

$$272 \quad q(x) = \int_{y_1}^{y_2} (V(x, y) - V_{bg}(x, y)) dy \quad (4)$$

273 where $(V(x, y) - V_{bg}(x, y))$ represents the NO₂ enhancement above the background in kg m⁻². To compute this and account
274 for missing satellite pixels, *ddeq* fits a Gaussian function to all GEMS pixels within a plume polygon:

$$275 \quad g(y) = \frac{q}{2\sqrt{\pi}\sigma} \exp \exp \left(-\frac{(y - \mu)^2}{2\sigma^2} \right) + my + b \quad (5)$$

276 Here, μ and $\sigma(x)$ are the plume center and width in meters, and $my + b$ approximates a linear background. The plume width
277 is further defined as:

$$278 \quad \sigma(x) = \sqrt{\frac{2Kx^\kappa}{u}} \quad (6)$$

279 Where K is the eddy diffusivity coefficient (m² s⁻¹), κ accounts for nonlinear plume spreading under varying meteorology, and
280 u is the effective transport wind speed defined above. The plume width, $\sigma(x)$ is derived from the Gaussian fit, and the
281 parameters, K and κ are then determined by fitting, $\sigma(x)$ within the CSF framework. After fitting the Gaussian function, line
282 densities are converted to fluxes using wind speeds at each corresponding downwind cross-section. Fluxes can be estimated
283 for several cross-sections or polygons located downwind of the urban source (see Fig. S1,S2) (Kuhlmann et al., 2024). Using
284 multiple points along the plume ensures different portions of the plume are sampled robustly.

286 3.1.3. Emission rate and lifetime estimation

287 Because NO₂ decays as the plume travels, the flux decreases with distance. To estimate the true emission rate, Q , at the source,
288 *ddeq* fits a lifetime τ by matching modeled and observed flux decay:



289
$$F_a(x, \tau, \mu_a, \sigma_a) = Q \int_{-\infty}^{\infty} D(x', \tau) g(x - x', \mu_a, \sigma_a) dx' \quad (7)$$

290 Where μ_a and σ_a describe the city-scale plume location and extent, $D(x', \tau)$ describes the exponential decay along the plume,
291 and g is the Gaussian parameter described above. Fitting Eq. (7) to the derived fluxes yields both the emission rate Q and
292 plume lifetime τ (Kuhlmann et al., 2024).

293

294 3.1.4. Conversion from NO₂ to NO_x emissions

295 GEMS provides NO₂ column densities; therefore, a NO₂-to-NO_x conversion factor is needed to obtain NO_x emissions.
296 Following the *ddeq* implementation, we use:

297
$$Q_{NO_x} = f_q \cdot Q_{NO_2} \quad (8)$$

298 to obtain NO_x estimates, where $f_q = 1.32$, as implemented in the *ddeq* algorithm.

299

300 3.2 GEMS-derived NO_x emission estimates

301 GEMS NO_x emissions for Bangkok were estimated for daytime hours (00:45:00 – 06:45:00 UTC) during the ASIA-AQ
302 deployment, 14 – 27 March 2024. Days with significant cloud contamination were removed from the analyses on a case-by-
303 case basis, leaving emissions estimates for 14,15,17,18,22,24,25 March 2024. Emissions were computed for both weekends
304 and weekdays, however, due to fewer weekends in the study period, weekday estimates are estimated to be more robust. We
305 aggregate emissions hourly across weekdays to produce a summary daytime profile as illustrated in Fig. 3a. Emissions
306 generally range between 0.5 – 4 kg s⁻¹ dependent on the inversion method. Differences between CSF, GP, and IME emission
307 estimates are expected, as each method relies on distinct assumptions regarding transport, plume geometry, and chemical loss.
308 Similar spreads between methods have been reported in previous satellite-based emission studies (Hakkarainen et al., 2023,
309 2024; Santaren et al., 2025), particularly in urban environments, and can be interpreted as a measure of structural uncertainty
310 rather than inconsistency between methodologies. Nevertheless, in this application, the CSF method illustrates a distinct
311 daytime pattern with emissions peaking at 01:00:00 UTC (or 08:00:00 LT) coinciding with morning rush hour traffic,
312 decreasing by approximately 65% by 14:00:00 LT. The GP and IME results illustrate a relatively stable daytime pattern and
313 overall lower (< 50%) morning emission compared to the CSF method.

314

315 3.3 Selection of the inversion method

316 To identify the optimal inversion method to be used for model correction, we test which method can successfully recover
317 WRF-Chem's prior daytime NO_x emission profile. To do so, we apply the *ddeq* inversion algorithms to WRF_{Base}. To replicate
318 the satellite output, we re-gridded the model output from its native resolution to the satellite swath grid using the Universal



319 Regridder for Geospatial Data (xESMF) Python package (Jiawei Zhuang et al., 2025). A nearest-neighbor interpolation scheme
320 was used to preserve spatial gradients and align the model resolution to that of the satellite observations. This spatial re-
321 gridding was performed on an hourly basis, corresponding to the nearest observation time (00:45:00 – 06:45:00 UTC).
322 Following re-gridding, model NO₂ mixing ratios were vertically interpolated to the satellite pressure levels using a one-
323 dimensional linear interpolation to ensure consistency between the model and observed data for averaging kernel application.
324 After interpolating model output to GEMS’s spatial and pressure grid, we computed the model’s tropospheric column NO₂
325 (molecules cm⁻²). This is done by converting the model’s standard output of NO₂ volume mixing ratio (ppmV) to a number
326 density with the ideal gas law:

$$327 \quad NO_{2_{Number\ Density}} = \frac{P \cdot \chi_{NO_2} \cdot N_A}{R \cdot T} \quad (9)$$

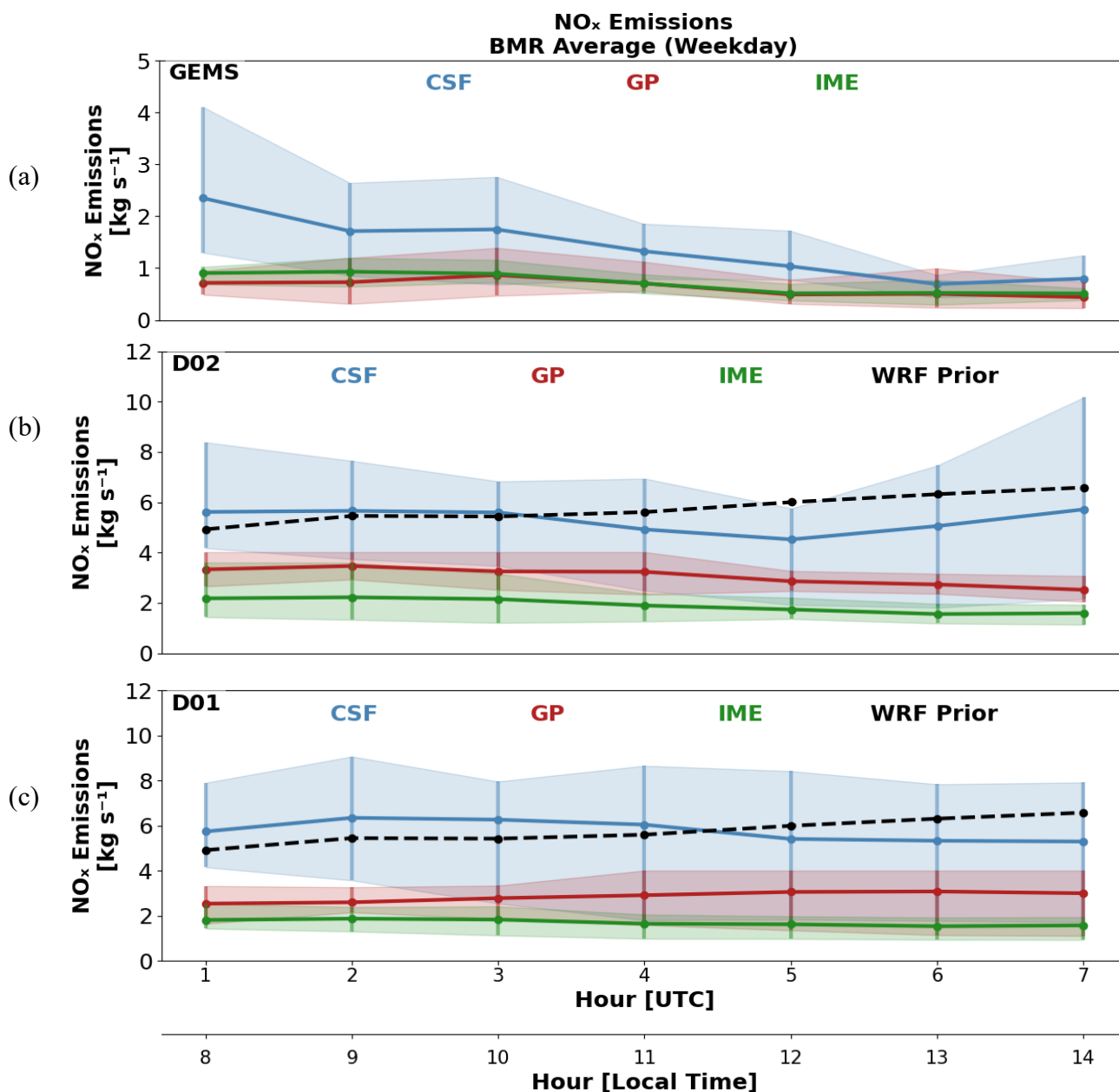
328 Where χ_{NO_2} is the NO₂ mixing ratio in ppmV, P is pressure in Pa, T is temperature in K, R is the gas constant (8.314 J/mol/K),
329 and N_A is Avogadro’s number ($6.022 \times 10^{23} \text{ mol}^{-1}$). The number density is then multiplied by the thickness of each vertical
330 model layer Δz to obtain the NO₂ amount per unit area. Summing across all layers yields the total column NO₂:

$$331 \quad NO_{2_{WRF-GEMS}} = \frac{1}{10^4} \times \sum_k (A_k \cdot NO_{2_{Number\ Density,k}} \cdot \Delta z_k) \quad (10)$$

332 Where A_k is the averaging kernel value at layer k , Δz_k is the thickness of the model layer k , in meters, and $\frac{1}{10^4}$ converts the
333 units to molecules cm⁻². As WRF-Chem has no stratosphere, we regard this as the tropospheric column NO₂. The satellite
334 averaging kernel weights each model layer based on how sensitive GEMS is to that part of the atmosphere. This allows for a
335 direct comparison with GEMS retrievals.

336
337 We compute NO_x emissions from re-gridded WRF_{Base} (which we denote as WRF-GEMS) with *ddeg* and the resulting average
338 daytime profile for Bangkok is illustrated in Fig. 3b, 3c. The model’s shape and magnitude of NO_x emissions differ
339 substantially from the GEMS emission data. Model emissions are initially > 50% larger than GEMS-derived emissions.
340 Additionally, there are minimal changes in the daytime pattern present in any of the inversion methods. In fact, WRF-GEMS
341 D02 sees an increase in emission between 08:00:00-10:00:00 LT, a pattern that disagrees with the observed satellite emissions.
342 The results here further illustrate the need for an hourly correction to the model’s emission profile, rather than applying a single
343 scaling factor across all hours. The WRF_{Base} prior emission profile is shown by the black dashed line. For this comparison, we
344 smoothed the prior emission profile using a 3 h backward-looking average to account for the accumulation and chemical
345 evolution represented implicitly in the inversion results. Overlaying the prior emissions shows that the CSF method most
346 accurately recovers them. As a result, we select the CSF inversion method moving forward to correct and scale WRF-Chem’s
347 daytime NO_x emission profile.

348



349
 350 **Figure 3.** Comparison of daytime NO_x emission estimates derived from (a) GEMS, (b) WRF-GEMS D02, and (c) WRF-
 351 GEMS D01 using the Cross-Sectional Flux (blue), Gaussian Plume inversion (red), and Integrated Mass Enhancement (green)
 352 methods. Emissions (kg s⁻¹) represent averages across daytime hours and weekdays during the ASIA-AQ deployment period
 353 (14 – 27 March 2024). Model inversion emissions in (b) and (c) were obtained by re-gridding WRF_{Base} output to the GEMS
 354 spatial resolution and applying the same inversion methods. The WRF_{Base} prior emission profile is shown as a black dashed



355 line and represents a backward-looking three-hour average to account for emission accumulation embedded in the inversion
356 estimates.

357

358 **4 Model emission adjustment framework**

359 To better represent NO_x emissions over Bangkok, we developed an optimization framework to re-scale and shape WRF-
360 Chem's input daytime emissions across the BMR (see step 2 Fig. 2). The prior emissions come from monthly EDGAR v5
361 values. The optimization uses a cost function $J(x)$ to adjust daytime model emissions based on GEMS NO_x retrievals,
362 incorporating the lifetime and uncertainties from both the model and observations.

363 **4.1 Optimization of daytime anthropogenic NO_x emissions**

364 **4.1.1. Observational constraint**

365 The GEMS average daytime NO_x profile (blue line in Fig. 3a) from the CSF method provides the observational constraint. To
366 improve consistency between the observed and modeled columns, we applied a correction factor to the constraint to account
367 for the portion of the NO₂ column that GEMS does not capture because of reduced sensitivity near the surface. Although the
368 air mass factor (AMF) calculation includes vertical weighting, the retrieved GEMS column can still underestimate tropospheric
369 NO₂ in conditions where a substantial fraction resides in the lowest few hundred meters and is weakly sensed by the instrument.
370 To address this sensitivity, GEMS-derived NO_x emission estimates were scaled using the ratio of WRF-Chem emissions
371 obtained from the full column (i.e., Eq. (10) excluding the A_k) and from the same column after application of the GEMS
372 averaging kernel:

$$373 \quad y = e_{GEMS} \times \left(\frac{e_{WRF}^{TC}}{e_{WRF}^{AK}} \right) \quad (11)$$

374 Where e_{GEMS} , e_{WRF}^{TC} , and e_{WRF}^{AK} denote the CSF-derived daytime NO_x emission profiles derived from GEMS, WRF-Chem
375 (D02) total columns, and the same columns after applying the GEMS averaging kernel, respectively. Hourly correction factors
376 ranged between 1.05 – 1.33, where larger corrections (e.g., 1.33) were present in the morning hours, 01:00:00 – 02:00:00
377 UTC. This vertically adjusted emission vector was used as the observational constraint, y , in the optimization.

378

379 **4.1.2. Prior assumptions, lifetimes, and temporal weighting**

380 The prior for the optimization, x_b , refers to the bottom-up daytime NO_x emission profile shown in the black dashed line in Fig.
381 3b. For the optimization, it is necessary to map the model emissions to the satellite-derived emissions through the observational
382 operator H . Satellite emissions of NO_x represent not only emissions from the current hour, but also contributions from
383 preceding hours. To address this, we introduce an operator H that links the model daytime hourly emissions to the observed



384 GEMS NO_x amounts. Each row of H defines how emissions from a set of prior model hours contribute to an observation at
385 time, t_i .

386

387 For each GEMS observation hour t_i , we assume that the column enhancement is influenced by emissions from a backward-
388 looking window of three model hours:

389

$$t_i - 2, t_i - 1, t_i$$

390 The window choice was determined by comparing inversion results to model priors using averaging windows from 1 – 6 hours.

391 The three-hour window provided the best agreement with the CSF inversion as shown in Fig 3b, 3c. Within this window, the

392 contribution from each prior hour depends on the atmospheric lifetime of NO₂ for that hour. We use hourly lifetimes, τ , from

393 GEMS which were fitted within the CSF inversion in Eq. (7). WRF-Chem-derived decay times are generally longer than those

394 inferred from GEMS, with partial overlap at earlier hours but increasing divergence later in the day, indicating differences in

395 the effective loss and dilution processes represented by the model. Hours with no satellite information, are assigned a default

396 lifetime of 3 hours. We then apply a simple exponential decay law:

397

$$w(\Delta t) = \exp\left(-\frac{\Delta t}{\tau}\right) \quad (12)$$

398 where:

399

$$\Delta t \in \{0,1,2\}$$

400 is the time lag between when NO_x was emitted and when its NO₂ enhancement is observed. These raw weights are normalized

401 within each row of H to ensure mass conservation:

402

$$H_{i,j} = \frac{w(\Delta t_j)}{\sum_{j'} w(\Delta t_{j'})} \quad (13)$$

403 Thus, $H_{i,j}$, represents the fraction of the observed column at hour i , that is attributable to emissions from model hour j . This

404 framework of H ensures that shorter lifetimes contribute to a stronger emphasis on the most recent emissions, appropriately

405 reflecting rapid chemical loss, and longer lifetimes spread the influence of emissions over multiple hours, consistent with

406 slower decay. By embedding this chemical persistence into the operator, H , we obtain a physically representative mapping

407 between model emissions and the satellite observations that are used to constrain them.

408

409 4.1.3. Solution for optimized daytime emissions

410 A model corrected daytime NO_x emission profile, \hat{x} was obtained by minimizing the following cost function:

411

$$J(x) = \frac{1}{2}(y - Hx)^T R^{-1}(y - Hx) + \frac{1}{2}(x - x_b)^T B^{-1}(x - x_b) \quad (14)$$

412 Where y is the GEMS, column-corrected NO_x emission vector, x is the unknown corrected model daytime emission profile,

413 x_b is the model prior profile, $R = \sigma_I^2 I$, $B = \sigma_B^2 I$ are the observation and background error covariance matrices, and H is the

414 observational operator matrix described above. In this study, we use $R = 1$ and $B = 10$. These values were based on sensitivity



415 tests in which we vary R and B over several orders of magnitude. The chosen values represent a compromise that allowed
416 the optimized emission profile to closely follow the satellite constrains while preventing excessive deviations from the prior
417 emission profile. To account for temporal correlation in prior emission errors, the elements of B are defined as:

418
$$B_{i,j} = \sigma^2_B \exp\left(-\frac{|t_i - t_j|}{L}\right) \quad (15)$$

419 Where $|t_i - t_j|$ is the temporal separation between emission hours i and j , and L is the temporal correlation length, set to $L =$
420 2 hr in this study. This setup ensures that prior errors vary smoothly in time rather than independently hour-to-hour. Finally,
421 the cost function was minimized using a Sequential Least Squares Quadratic Programming (SLSQP) algorithm
422 (minimize(method='SLSQP') — SciPy v1.16.2 Manual, 2025; Nocedal and Wright, 2006). The result is a corrected model
423 hourly emission vector, \hat{x} , that balances the satellite observations with the model's prior estimate while accounting for
424 chemistry and transport behavior (Fig. 4).

425
426 Figure 4a illustrates the raw hourly daytime NO_x for both the prior model (dashed purple) and optimized version (solid purple).
427 The optimized profile departs notably from the prior in both magnitude and shape, with a pronounced morning peak at 07:00:00
428 LT, followed by a steady decline until 13:00:00 LT. This pattern is consistent with temporal patterns in weekday traffic
429 intensity in Bangkok found in Ly et al. (2015), which found the morning traffic to peak at 07:30:00 LT ending at 09:30:00 LT,
430 and the evening peak from 17:00:00 to 20:00:00 LT (outside of GEMS observing window). Activity begins to increase at 13:00
431 LT which corresponds to the NO_x increase we begin to see in the optimized result after 06:00:00 UTC. When the prior and
432 optimized hourly emissions are passed through H , we obtain a temporally smoothed emission profile consistent with what
433 GEMS would observe (Fig. 4b). Figure 4b shows the optimized profile closely reproduces the GEMS-derived daytime pattern,
434 indicating the optimization effectively aligns model emissions with satellite observations while preserving components of the
435 prior model behavior.

436 4.2 Adjustment of WRF-Chem diurnal emission profiles

437 Using GEMS-derived NO_x emissions and the optimization results above, we correct the WRF-Chem 24 h input emissions over
438 the BMR. Since GEMS provides estimates over 01:00:00-07:00:00 UTC, we only have optimized model emissions over this
439 window. To apply these updates to the full gridded 24 h WRF-Chem anthropogenic emission input (00:00:00-23:00:00 UTC),
440 while preserving the model's spatial distribution, we compute hourly scaling factors which we use to adjust the gridded input
441 NO_x emissions.

442
443 To compute the factors, hourly WRF-Chem NO and NO_2 emission fields were summed across the vertical levels and masked
444 to the Bangkok region bounded by N-S:13.5°-15.0°, W-E:100.2°-100.9°, using the WRF-Chem grid. In WRF-Chem, NO_x
445 emissions are stored as NO_2 -equivalent mass (' NO_x -as- NO_2 '), so all conversions use the molecular weight of NO_2 . The total
446 emissions were converted to mol hr^{-1} using a molecular weight of 46.01 g mol^{-1} and an area of 16 km^2 per grid cell (following

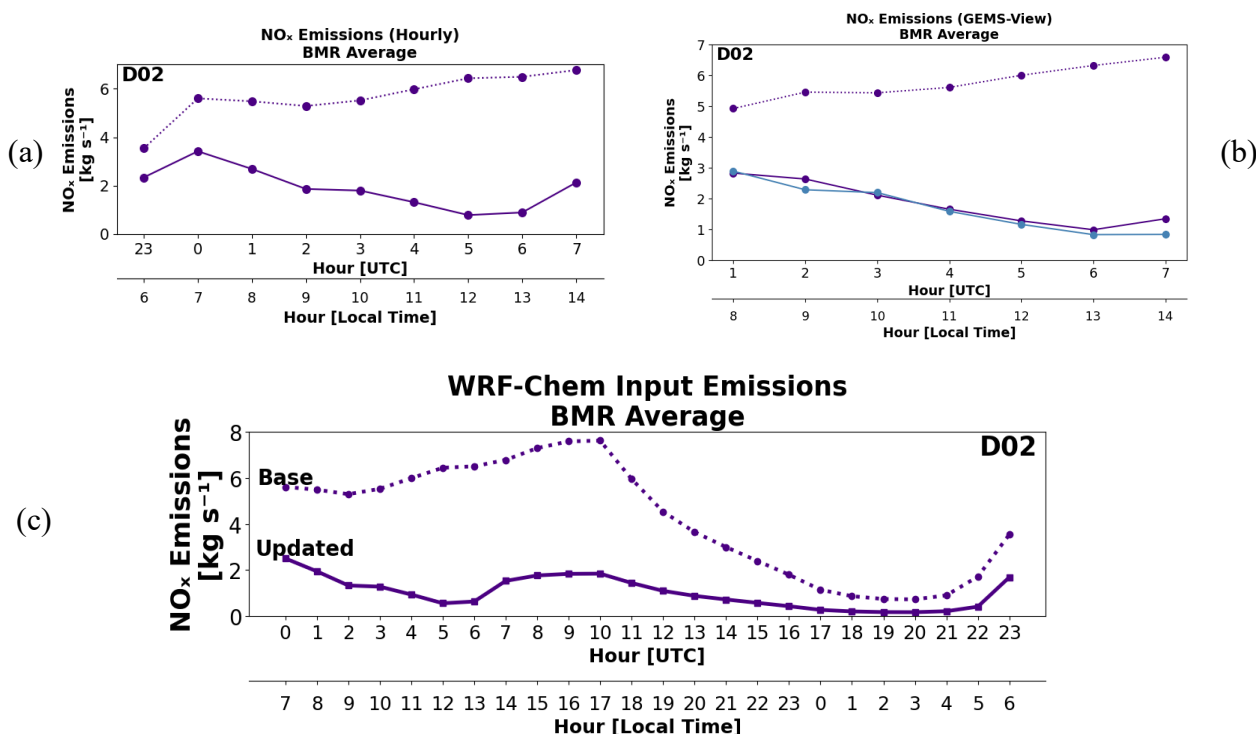


447 the resolution of D02). Each optimized emission, \hat{x}_h was converted from kg s^{-1} to mol hr^{-1} and divided by the corresponding
 448 original WRF-Chem total to compute a scale factor, f for each hour h :

449
$$f = \frac{\hat{x}_h \times \frac{1000}{46.01} \times 3600}{E_H^{WRF}} \quad (16)$$

450 Where E_H^{WRF} is the original domain-integrated NO_x emissions for hour h . Since the optimization covered hours with GEMS
 451 measurements, the scaling factors for the remaining model hours were computed using the ratio of average daytime emissions
 452 where averages are taken over the constrained hours. Finally, we apply the scaling factors spatially over the BMR. The scaling
 453 factor was applied to the hourly WRF-Chem anthropogenic emissions input files and only to NO and NO_2 grid cells within the
 454 BMR mask. This preserves the original spatial distribution but adjusts the total emissions to match the optimized values. The
 455 updated emission files were then used to initialize an updated model simulation, ran for the ASIA-AQ deployment period,
 456 which we will refer to as $\text{WRF}_{\text{Updated}}$ (see step 3 Fig. 2).

457
 458 Figure 4c compares the average diurnal prior profile over BMR with the updated profile derived from the optimization and
 459 scaling procedure. The updated profile shows a notable increase in NO_x between 07:00:00-10:00:00 UTC (14:00:00 to 17:00:00
 460 LT), which may reflect the beginning of a rush-hour signal over the city. Nighttime emissions retain the overall shape of the
 461 prior profile but are scaled downward based on the daytime average. Figure S4 maps the spatial distribution of these updates
 462 across BMR, showing the largest differences in the late afternoon and early evening, with localized reductions of up to 400
 463 $\text{mol km}^{-2} \text{hr}^{-1}$ in the updated input emissions.





465 **Figure 4.** Results of the emissions optimization, shown as averages over the BMR. (a) Comparison of optimized (solid) and
466 prior (dashed) daytime NO_x emissions. (b) Same as (a) but viewed through the GEMS observational operator. The GEMS
467 profile is shown in blue. (c) Comparison of full optimized (solid) and prior (dashed) diurnal NO_x emission profiles.

468

469 **4.3 Comparison with bottom-up emission inventories**

470 To place the updated NO_x emissions in context of existing emission inventories, we compared total monthly emissions over
471 the BMR against several widely used bottom-up inventories, our top-down emissions, and emissions from a chemical
472 reanalysis product (Fig. 5). These include HTAP v3.2 (base 2019), a local Thailand Inventory (THAI-KMUTT) (base 2019),
473 MIX v2.3 (base 2017), EDGAR v5 (base 2015), CEDS (base 2024), our study (2024), and the Tropospheric Chemistry
474 Reanalysis (TCR-3) top-down emissions TCR-3 (2024) (Miyazaki et al., 2020). Across inventories, monthly totals for March
475 can vary nearly by an order of magnitude, highlighting large uncertainty in regional NO_x sources and emissions processing
476 methodology. For example, although both HTAP v3.2 and MIX v2.3 rely on the REAS framework (Kurokawa and Ohara,
477 2020) for Asian anthropogenic emissions, they are derived from different REAS versions, temporal coverage, and processing
478 assumptions, which can lead to substantial differences in absolute emission magnitudes over Bangkok. HTAP v3.2 is based
479 on REAS v3.2.1, which provides monthly emissions for 2000–2015 at a spatial resolution of 0.25° . In the HTAP product, these
480 emissions are re-gridded to 0.1° by assuming a uniform spatial distribution within each grid cell (Guizzardi et al., 2025). In
481 contrast, the MIX inventory is based on REAS v2, which covers 2000–2008 and reflects earlier emission estimates and activity
482 data (Li et al., 2024). REAS v2 was subsequently extended to 2010 following the scaling approach described by Kurokawa &
483 Ohara (2020).

484

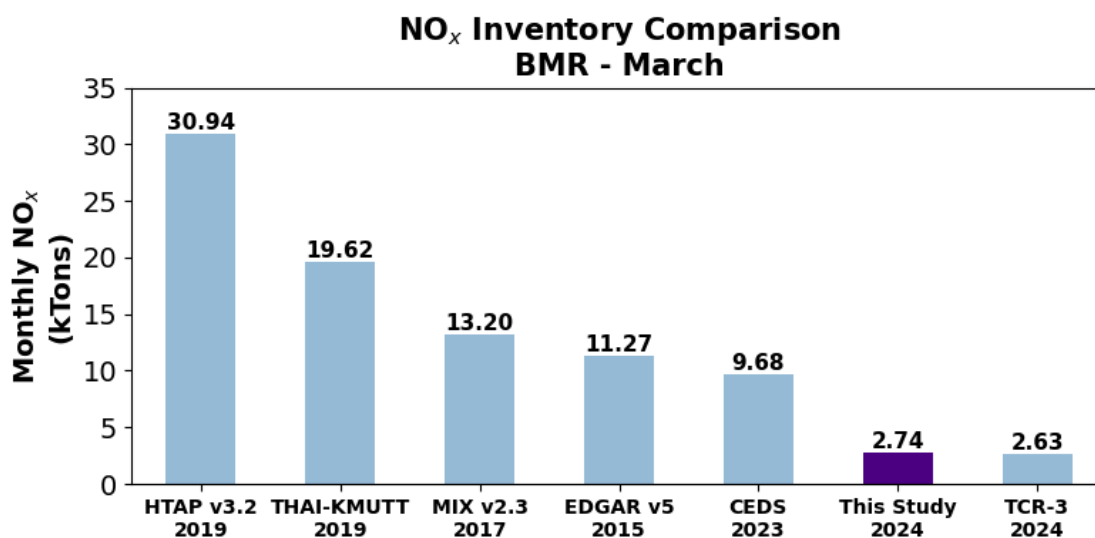
485 Overall, HTAP v3.2 depicts the highest NO_x totals at $31\text{kTons month}^{-1}$. THAI-KMUTT follows with emissions at $\sim 20\text{ kTons}$
486 month^{-1} , reflecting its incorporation of detailed regional activity from local emissions data. The coarser-resolution MIX v2.3,
487 and EDGAR v5, and CEDS inventories reflect lower totals, at $\sim 13, 11, 10\text{ kTons month}^{-1}$ respectively, consistent with the use
488 of different emission estimation methodology and older base years for MIX and EDGAR which correspond to lower macro-
489 economic (e.g., GDP) indicators in Thailand compared to 2019. Lastly, GEMS top-down NO_x estimates and TCR-3 estimates
490 based on the chemical reanalysis using TROPOMI NO_2 indicate substantially lower emissions ($2\text{--}3\text{ kTons month}^{-1}$). These
491 reduced magnitudes may result from both recent emission declines and structural differences in how emissions are computed
492 (i.e., top-down perspective).

493

494 It is important to note uncertainties are present and differ amongst emission methods. For example, bottom-up inventories
495 depend on activity data, emission factors, spatial approximations, and assumptions that may not capture rapid socio-economic
496 changes or region-specific behavior. Top-down estimates incorporate uncertainties from their respective satellite retrievals,
497 reanalysis data (e.g., ERA5), averaging kernels, chemical lifetime assumptions, and forecast-model transport and chemistry



498 (e.g., TCR-3). Together, these differences highlight the value of combining observational constraints with updated bottom-up
499 information to define NO_x emission estimates.
500



501
502
503 **Figure 5.** Comparison of March NO_x emissions over the BMR derived from bottom-up, top-down, and assimilated approaches.
504 Bottom-up inventories (HTAP v3.2 (Guizzardi et al., 2025), THAI-KMUTT, MIX v2.3 (Li et al., 2024), EDGAR v5 (Crippa
505 et al., 2020), and CEDS (Hoesly et al., 2018)) exhibit substantial variability. In contrast, top-down estimates from GEMS and
506 TROPOMI (TCR-3) for 2024 indicate considerably lower emissions (2.6–2.7 kt month⁻¹), highlighting uncertainties in bottom-
507 up inventory methodologies, satellite sensitivity, and potential changes in anthropogenic NO_x activity.
508

509 5 Evaluation against satellite observations

510 To evaluate the performance of WRF-Chem (Base + Updated) NO₂ simulations during the ASIA-AQ period (14 – 27 March
511 2024) in Bangkok, we first compared model output with satellite tropospheric column NO₂ retrievals from GEMS v3 data. For
512 GEMS observations, pixels were filtered based on cloud fraction (CF < 0.3). The GEMS averaging kernel and air mass factor
513 data were used to isolate tropospheric contributions and account for satellite instrument sensitivity. To enable a direct
514 comparison with our model output, we re-gridded model output from its native resolution to the satellite swath grid as explained
515 in Sect. 3.3. As before, refer to the re-gridded model simulations with the GEMS averaging kernel applied as WRF-GEMS.
516 To evaluate regional NO₂ variability, we aggregated satellite and model-derived tropospheric column NO₂ values over the
517 BMR, by defining a N-S (13.5-14°N), W-E (100.3-100.9°E) bounding box for the area. For pixels within this boxed region,
518 we calculate the mean NO₂ concentration, minimum NO₂, maximum NO₂, standard deviation, and the 10th and 90th percentiles



519 to characterize regional variability. This analysis was repeated on an hourly basis for each co-located WRF-Chem and GEMS
520 dataset, providing a regionally aggregated view of column NO₂ for intercomparison.

521

522 The maps shown in Fig. 6 illustrate a spatial comparison of (a) GEMS, (b) updated model results, WRF-GEMS_{Updated} D02, and
523 (c) base model, WRF-GEMS_{Base} D02 tropospheric columns NO₂ over the BMR for several snapshots on 18 March 2024.
524 Results for D01 can be found in Fig. S5, S6. GEMS generally places BMR city enhancements between $5 \times 10^{15} - 2 \times 10^{16}$
525 molecules cm⁻² in a N-S direction. Both WRF_{Updated} D01, D02 generally reflect the spatial distribution and magnitude of
526 tropospheric column NO₂ observed during daylight hours. WRF_{Updated} D02 (Fig. 6b) tends to place the city plume more
527 northward at 04:00:00 and 07:00:00 UTC compared to what is observed in GEMS data (Fig 6a). This spatial discrepancy is
528 likely related to overpredicted model winds (further discussed in Sect. 6.1) which displaces the plume in a northward direction.
529 Nevertheless, the daytime pattern seen in GEMS is accurately reflected in WRF_{Updated} with column NO₂ values at their peak in
530 the morning hours (08:00:00 LT), decreasing substantially throughout the afternoon (14:00:00 LT) due to photochemical
531 interactions. This is a substantial improvement from WRF_{Base}, which sees a large overestimation of NO₂ in the morning hours
532 followed by persistent and growing NO₂ columns throughout the afternoon as seen in Fig. 6c.

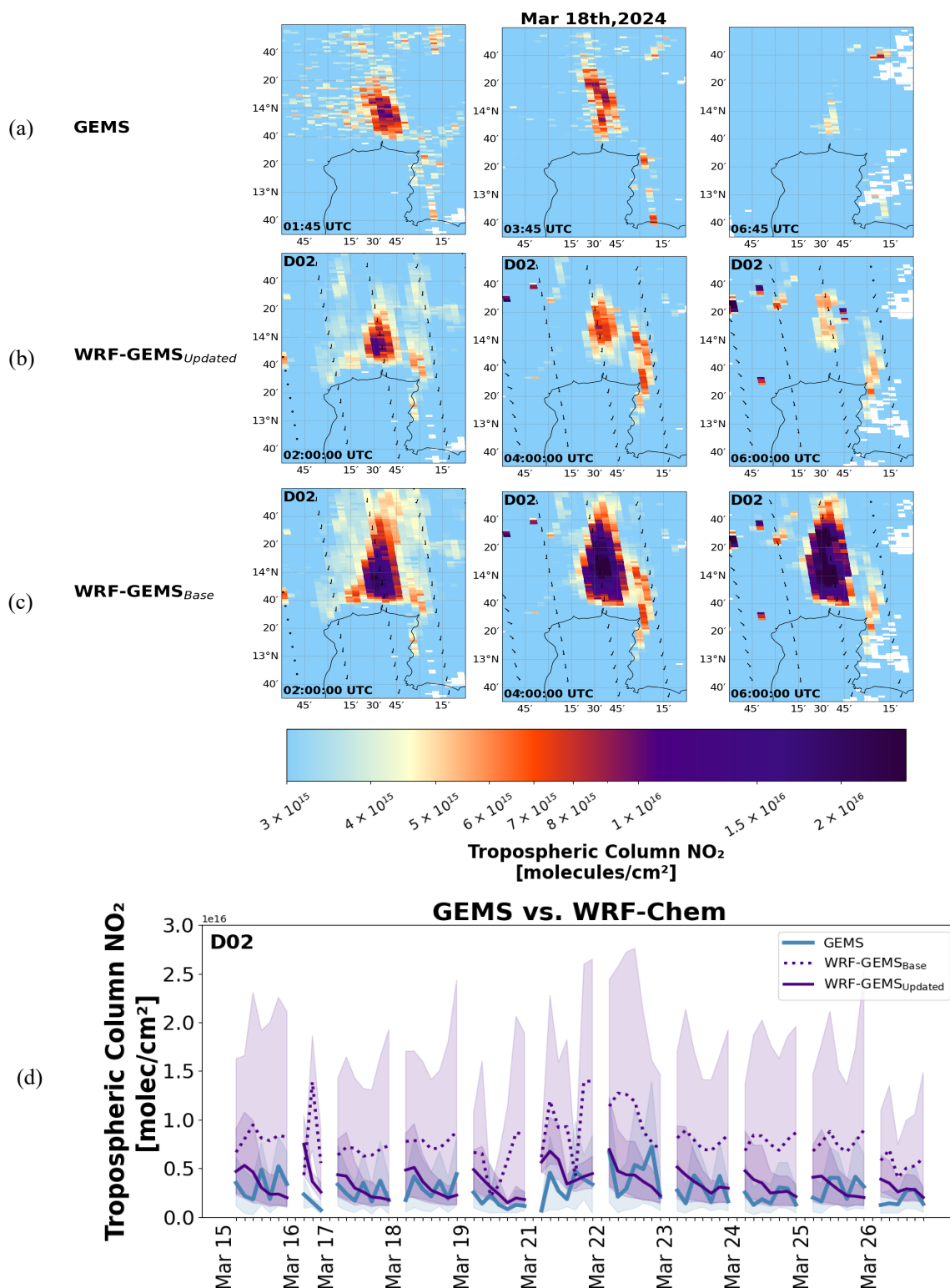
533

534 The time series in Fig. 6d illustrates a full comparison of daytime tropospheric column NO₂ values across model types in D02
535 (see Fig. S8 for D01) for the duration of ASIA-AQ. WRF-GEMS_{Updated} indicates a clear reduction in error and bias from
536 WRF_{Base} as illustrated by the reduced NO₂ columns and model spread. WRF_{Updated} also indicates corrected daytime patterns
537 compared to WRF_{Base}, indicating better consistency with GEMS observations for the deployment period with few exceptions
538 such as 22 March where GEMS has peaks in the afternoon (further discussed in Sect. 6.1).

539



540
 541





542 **Figure 6.** Spatial comparison over the BMR on 18 March 2024 of tropospheric NO₂ columns from (a) GEMS, (b) WRF-
543 GEMSU_{updated} D02, and (c) WRF-GEMSB_{ase} D02 for snapshots at 02:00:00, 04:00:00, and 07:00:00 UTC, corresponding to
544 approximately 09:00, 11:00:00, and 14:00:00 LT. (d) Tropospheric NO₂ column for daytime hours between GEMS (blue),
545 WRF-GEMSB_{ase} D02 (dotted purple), and WRF-GEMSU_{updated} D02 (solid purple) during the ASIA-AQ deployment period.
546 Shaded regions indicate variability, represented by the 10th and 90th percentiles.

547 **6 Evaluation using independent observations**

548 To independently assess the performance of the optimized WRF-Chem simulations, we compared model results for D01 and
549 D02 against a suite of independent airborne and ground-based observations distinct from the satellite measurements used in
550 the emission optimization process (see step 4 Fig. 2). This evaluation primarily emphasizes the results of D02 (4 km), which
551 more directly represents urban-scale processes and exhibits improved performance compared to D01 across multiple
552 observational datasets. These datasets provide an unbiased test of how well the model reproduces meteorological conditions
553 and trace gas amounts beyond those directly constrained from GEMS observations. By evaluating WRF-Chem against surface
554 monitoring networks (Thailand PCD), Pandora spectrometer measurements, and airborne ASIA-AQ data (e.g., GCAS NO₂
555 columns, DC-8 vertical profiles), we examine the model's ability to capture daytime variability, vertical structure, and surface
556 concentrations of NO₂ across different spatial and temporal scales. Evaluation amongst these diverse datasets, therefore, helps
557 to support the robustness of the emission correction framework described in this paper.

558
559 **Table 2.** Summary of WRF-Chem D02 validation statistics for WRF_{Base} (B) and WRF_{Updated} (U) simulations evaluated against
560 independent observational datasets. Metrics include mean bias (MB), mean error (ME), normalized mean bias (NMB),
561 normalized mean error (NME), root-mean-square error (RMSE), and Pearson correlation coefficient (CORR).

562
563
564
565
566
567
568
569
570
571
572



Dataset	Species	Model Run	MB	ME	NMB	NME	RMSE	CORR
GCAS	Tropospheric NO ₂ column (molecules cm ⁻²)	B	4.0E+15	5.1E+15	93	1.2E+2	9.3E+15	0.64
		U	-2.4E+14	1.9E+15	-5.6	45	3.4E+15	0.54
DC-8	NO _x O ₃ NO ₂ (ppbV)	B	1.3	1.4	82	87	2.8	0.97
		U	-0.81	0.8	-49	49	1.4	0.93
	CANOE NO ₂ (ppbV)	B	1.4	1.5	87	94	2.9	0.97
		U	-0.76	0.76	-48	48	1.3	0.93
Ground Monitors	NO ₂ (ppbV)	B	12	12	1.3E+2	1.3E+2	15	0.61
		U	-3.0	4.5	-32	47	5.6	0.53
	NO _x (ppbV)	B	14	15	1.4E+2	1.4E+2	18	0.59
		U	-3.6	4.9	-34	47	6.7	0.61
	O ₃ (ppbV)	B	-5.6	8.2	-18	27	10	0.87
		U	4.9	8.5	16	27	11	0.81
Pandora	Tropospheric NO ₂ column (molecules cm ⁻²)	B	7.9E+15	8.6E+15	55	59	9.6E+15	0.71
		U	-6.6E+15	6.8E+15	-46	47	8.2E+15	0.67

573

574 **6.1 Meteorological evaluation: winds and PBL height**

575 **6.1.1. Evaluation methodology**

576 To assess the performance of WRF-Chem meteorological fields, modelled wind speed and direction were evaluated against
 577 surface observations across the BMR during the ASIA-AQ campaign, 14 – 27 March 2024. Surface observations of wind speed



578 (m s⁻¹) and direction are obtained from Thailand Pollution Control Department (PCD) ground monitor network data. Hourly
579 surface wind observations from PCD network data were co-located with corresponding model outputs for D01 and D02. For
580 each site, model data were extracted from the nearest grid cell and interpolated to observation timestamps. Daily wind roses
581 were constructed to visualize and compare the frequency distribution of wind speed and direction between the model and
582 observations. For each station, wind speeds were binned into intervals of 0-1, 1-3, 3-5, and 5-8 m s⁻¹ and wind directions were
583 grouped into 16 compass sectors. Normalized frequency counts were computed to highlight dominant flow patterns. Data was
584 averaged across stations within a larger bounding box around BMR, N-S (12.5-15°N), W-E (99.5-101.5°E). For meteorology,
585 we use a large box that spans the regional flow influencing Bangkok so that we capture plume transport into and out of the
586 city. Figure S7a illustrates the station locations and averaging domains in Bangkok.

587
588 Additionally, we performed an evaluation of planetary boundary layer height (PBLH) to gauge the model's ability to capture
589 daily PBLH magnitude and development during the deployment period. Observed PBLHs were derived from airborne HSRL-
590 2 data following a machine learning approach described in Christopoulos et al., (2025) for ASIA-AQ flight days, 18 March,
591 19 March, 23 March, and 25 March 2024. We evaluate PBLHs for aircraft raster periods (i.e., Raster 1: morning, Raster 2:
592 afternoon, Raster 3: late afternoon/evening hours) and co-locate the observed PBLHs to modelled PBLHs based on a nearest
593 grid-cell approximation.

594

595 **6.1.2. Model-observation wind discrepancies**

596 Within the observational data, a pronounced synoptic transition occurred over Thailand on 20 – 21 March 2024, during which
597 winds reversed from the typical southwesterlies that were present during the deployment period to northeasterlies, weakened
598 substantially, coinciding with a drop in PBLH, and increased atmospheric stability (see PCD observations; Fig. S8-10). This
599 transition played a major role in PM_{2.5} and ozone exceedances by promoting stagnation over the BMR. The WRF-Chem
600 simulation failed to capture the timing or strength of this abrupt wind shift and associated stagnation (Fig. S8a, S8b). The
601 model instead maintained stronger southwesterly flow and higher PBLH, which led to unrealistic vertical mixing patterns
602 compared to the observations (Fig. S8-S10). Since this mismatch drives discrepancies between model and observations that
603 are unrelated to emissions adjustments/inversions, we exclude 20 – 21 March from the inversion/air quality evaluation.
604 Although the simulation is driven by FNL, it is possible for WRF-Chem to mis-time a rapid synoptic transition. This event
605 evolved on a relatively short spatial and temporal scale, and the coarse FNL boundary conditions may not have fully resolved
606 the sharp changes in low-level flow. In addition, local processes (i.e., convection, PBL mixing, land-sea interactions) around
607 Bangkok can cause the model to drift from the observed timing once it is integrated forward. We suspect these factors likely
608 contributed to the later wind shift in WRF-Chem. We additionally found WRF-Chem (D01, D02) systematically overpredicts
609 wind speed throughout the deployment (Fig. S8a, S8b; Table S2) with better agreement from the high-resolution 4 km domain.



610 This bias likely arises from that fact that many PCD monitors are embedded within the complex urban environment of
611 Bangkok, which are not fully resolved at WRF-Chem's spatial scale.

612

613 The consequences of this mis-timed synoptic transition are most pronounced on 21 March as demonstrated in the next section,
614 when weak large-scale flow made the simulation highly sensitive to local processes. Under these conditions, WRF-Chem
615 misses the stagnation and dilutes pollutants too quickly. This helps explain why the model performs worst during the highest
616 observed PM_{2.5} and O₃ episode. These results indicate that forecast performance during similar weak-flow pollution events
617 would benefit from improved representation of urban boundary-layer processes (e.g., surface roughness, urban canopy effects,
618 and land-sea breeze structure).

619

620 **6.1.3. Model-observation PBLH discrepancies**

621 As shown in Fig. S10 and summarized in Table S3, WRF-Chem generally captures the temporal evolution of the PBLH
622 observed by the aircraft. During the daytime (afternoon hours represented by Raster 2-3), the simulated PBL is broadly
623 comparable to the observations, with median values that are often similar. However, the magnitude and sign of the model bias
624 vary by day, with WRF-Chem demonstrating both over- and under- estimation likely related to the meteorological conditions.
625 This day-to-day variability suggests PBLH biases are not systematic during the afternoon and may influence surface pollution
626 dilation differently across individual cases, potentially contributing to variability in simulated daytime NO₂ concentrations
627 rather than a consistent model bias.

628

629 **6.2 Surface air quality evaluation**

630 To evaluate model performance of surface trace gases, modelled surface mixing ratios of NO₂, NO_x, and O₃ were evaluated
631 against observations across BMR during 14 – 27 March 2024. Surface observations of these constituents (in ppbV) were
632 obtained from Thailand PCD ground monitor network data. Like the evaluation of wind speeds and direction, data was co-
633 located by extracting model information from the nearest grid cell and matched to the observation timesteps. Station data and
634 model data were averaged across stations located within the Bangkok urban plume, bounded by N-S (13.5-14.6°N), W-E
635 (100.2-101°E). Figure S7b illustrates the station locations and averaging domain in Bangkok. For the air quality evaluation,
636 we restrict the station averaging domain to a smaller area over the Bangkok urban plume. This smaller domain allows us to
637 assess how the inversion and optimization specifically correct the local plume structure as opposed to a broader regional
638 background.

639



640 6.2.1. NO₂ and NO_x

641 Figure 7a,7b,7c shows a comparison of average surface NO₂, NO_x, and O₃ (ppbV) for stations located within the Bangkok
642 urban plume during the ASIA-AQ deployment for D02. D01 results are available in Fig. S11. The 20 – 21 March is shaded in
643 grey to indicate the period where the model mis-represented synoptic conditions resulting in enhancements in the observed
644 concentrations due to stagnation. During this time, NO₂, NO_x, and O₃ reached as high as 49, 59, and 103 ppbV, respectively.
645 Excluding this event, observed NO₂ and NO_x for this period generally ranged between 3 – 17 ppbV, and 3.5 – 22 ppbV
646 respectively. Overall, there is a clear improvement in the representation of NO₂ and NO_x during this period in WRF_{Updated} as
647 shown in Fig 7a, 7b. Table 2 depicts summary statistics for this analysis. The baseline simulation, WRF_{Base} overestimates both
648 NO₂ and NO_x with mean biases of +12 ppbV and +14 ppbV, respectively. With updated emissions, these large positive biases
649 in WRF_{Updated} were eliminated and reversed, yielding mean biases of -3.0 ppbV for NO₂ and -3.6 ppbV for NO_x. The remaining
650 negative bias is likely linked to the overprediction of winds, associated advection, and inversion related biases, which leads to
651 locally diluted concentrations near urban sites as shown in the previous analyses. Correlations with observed NO₂ and NO_x
652 remain moderate ($r = 0.5-0.6$) reflecting potential spatial discrepancies in WRF_{Updated} as seen in the previous analyses.

653

654 6.2.2. O₃

655 Observed O₃ generally ranged between 14–57 ppbV, excluding the stagnation event on 20 – 21 March, and the baseline model
656 captures this range reasonably well (Fig. 7c). After updating the emissions, O₃ increases in WRF_{Updated} primarily at night,
657 consistent with reduced NO titration following the decrease in NO_x emissions. Average diurnal cycles in D02 (Fig. S12a) show
658 that daytime O₃ production changes only modestly between base and updated simulations, indicating the emission update
659 mainly affects nighttime chemistry, as opposed to shifting photochemical O₃ formation in the daytime. This pattern is reflected
660 in the change in overall mean bias in Table 2, which shifts from an underprediction (-5.6 ppbV) to an overprediction (+4.9
661 ppbV).

662

663 The relatively weak daytime O₃ response to decreased NO_x emissions is consistent with recent analyses of O₃ formation
664 sensitivity during ASIA-AQ with in situ measurements, which indicate that the BMR exhibits mixed sensitivity to NO_x and
665 VOCs, in contrast to the predominantly NO_x-limited regimes observed at other ASIA-AQ locations (e.g., Manila) (Cho et al.,
666 2026). In this mixed-sensitivity regime, changes in NO_x emissions alone are not expected to strongly perturb daytime O₃
667 production, further providing validation for the minimal daytime O₃ response observed here. The magnitude of the daytime O₃
668 response varies by domain/model as shown by the D01 results (Fig. S12b). Although WRF_{Updated} D01 better matches observed
669 daytime O₃, this apparent improvement likely reflects NO_x titration associated with spatial dilution.

670



671 Overall, these results suggest that while the updated emissions improve the model's NO_x representation, further improvements
672 in VOC representation and local mixing processes may be needed to fully capture daytime O₃ levels in the BMR. Nevertheless,
673 the updated emissions substantially improve the model's simulation of surface NO₂ and NO_x, resulting in a more realistic
674 overall representation of air quality in Bangkok.

675

676 **6.3 Evaluation with Pandora column observations**

677 We additionally evaluate modelled NO₂ columns against Pandora measurements for the Bangkok site. Figure 7d depicts a
678 comparison of WRF_{Base} (light purple), WRF_{Updated} (dark purple), and Pandora (pink), tropospheric NO₂ column measurements
679 for days with high quality data. Throughout this period, Pandora measurements generally ranged between approximately $7 \times$
680 10^{15} – 3.5×10^{16} molecules cm⁻² and fit between WRF_{Base} which places columns higher (e.g., up to 5×10^{16} molecules cm⁻²)
681 and WRF_{Updated} which places columns lower (e.g. 2×10^{15} molecules cm⁻²). Average statistics between model cases for this
682 analysis are shown in Table 2. Biases are generally similar between model cases. WRF_{Base} overestimates column NO₂ as
683 illustrated by the mean bias ($+7.9 \times 10^{15}$ molecules cm⁻²) whereas emissions updates contribute to an underestimation ($-6.6 \times$
684 10^{15} molecules cm⁻²). However, there are some improvements in absolute error metrics with ME and RMSE decreasing by
685 roughly 20% and 12% respectively, and NME dropping from 61% to 48%. Figure S14 illustrates the spatial distribution of
686 mean tropospheric model NO₂ bias for GEMS and Pandora during the time reflected in Fig. 7d. In the WRF_{Base} simulation, a
687 strong positive bias is seen within and north of the Pandora site, indicating the overestimation of NO₂ columns (up to 2×10^{16}
688 molecules cm⁻²) in the urban plume relative to GEMS. This pattern reiterates the point that the prior anthropogenic emissions
689 (based on EDGAR v5) were too large with pollutant accumulation occurring downwind of Bangkok as a result. After applying
690 the emission updates, the WRF_{Updated} simulation essentially eliminates this bias. The overall bias near the Pandora site becomes
691 close to neutral or slightly negative, demonstrating the optimization effectively corrected the spatial overprediction. The
692 remaining negative bias close to the city center/Pandora site is likely related to discrepancies in the WRF_{Updated} urban plume
693 placement, overpredicted wind speeds, and inversion biases related to the GEMS retrievals. Daily biases for WRF_{Base} D01,
694 D02, and WRF_{Updated} D01, D02 can be found in Fig. S15 and Fig. S16.

695

696

697

698

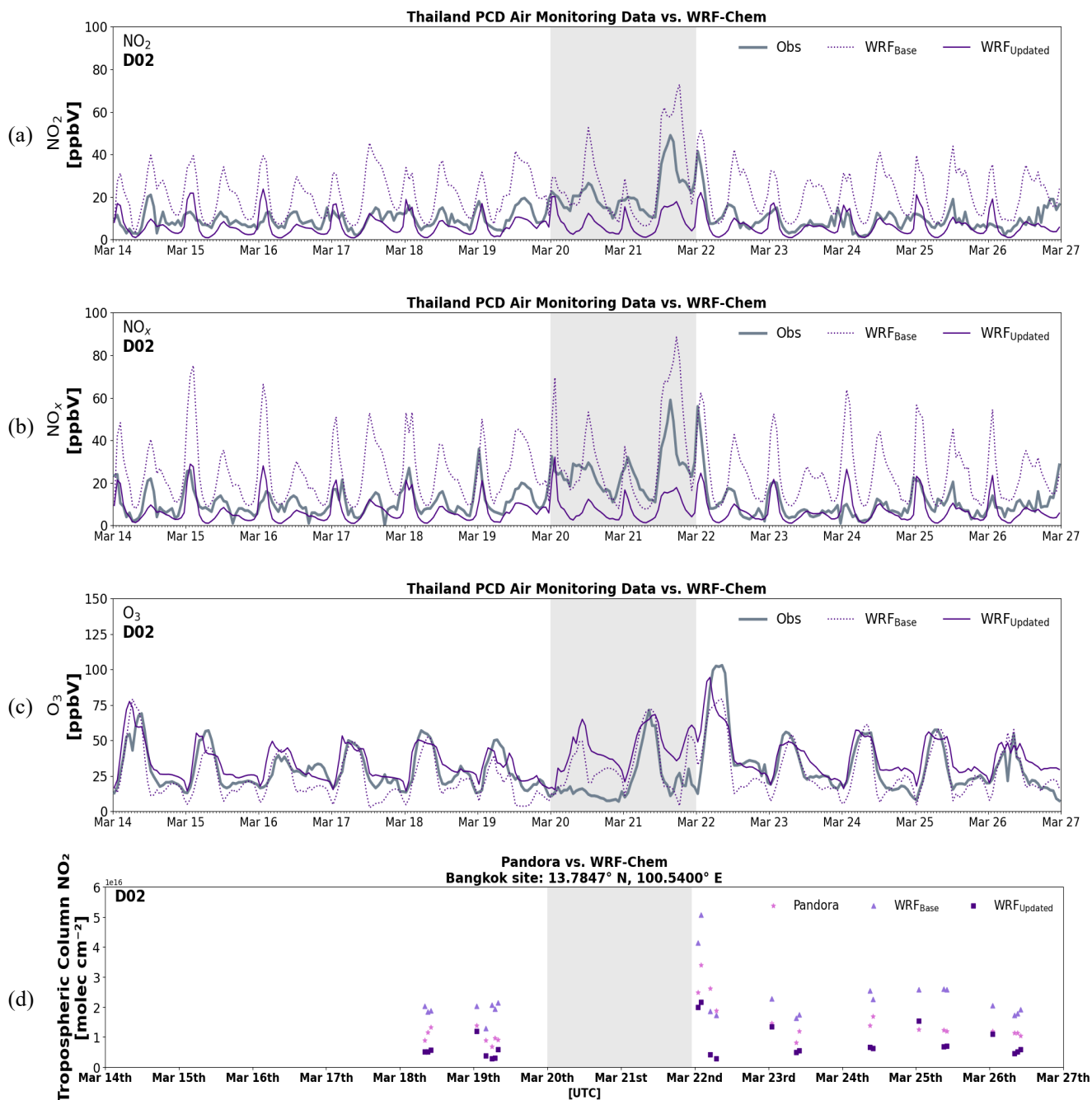
699

700

701

702

703



704
705
706
707
708

Figure 7. Comparison of WRF_{Base} D02 (dotted purple) and WRF_{Updated} D02 (solid purple) simulations against Thailand Pollution Control Department (PCD) ground-monitor network observations for (a) NO₂ mixing ratio (ppbv), (b) NO_x mixing ratio (ppbv), and (c) O₃ mixing ratio (ppbv) during the ASIA-AQ deployment period (14–27 March 2024). represent averages



709 across stations within the Bangkok urban plume. (d) Comparison of tropospheric NO₂ columns from WRF_{Base} D02 (light
710 purple), WRF_{Updated} D02 (dark purple), and Pandora (pink) for high-quality observations during the ASIA-AQ deployment
711 period (18 – 27 March 2024). The shaded region represents the stagnation period, 20 – 21 March excluded from the evaluation.
712

713 **6.4 Evaluation with ASIA-AQ aircraft measurements**

714 The Airborne and Satellite Investigation of Asian Air Quality (ASIA-AQ) was a NASA field campaign conducted in February
715 – March 2024 to advance the understanding of urban and regional air quality across East and Southeast Asia. Targeting several
716 megacities (e.g., Manila, Seoul, Bangkok, Chiang Mai), the campaign combined satellite observations, aircraft measurements,
717 ground-based monitoring, and modeling approaches to characterize pollution sources and validate satellite retrievals. A main
718 objective of ASIA-AQ was to evaluate the data from GEMS. Airborne observations were collected using the NASA DC-8 in
719 situ and LaRC G-III remote sensing aircraft, with coordinated support from ground-based networks such as Pandora and
720 AERONET. Additionally, chemical transport models (e.g., GEOS-Chem, GEOS-FP, MUSICA, WRF-Chem, WRF-CMAQ)
721 played a key role in real-time flight planning and post-campaign interpretation.
722

723 **6.4.1. GCAS**

724 The GEOstationary Coastal and Air Pollution Events (GEO-CAPE) Airborne Simulator (GCAS) is an airborne UV-Vis
725 spectrometer that was flown on the G-III aircraft during the ASIA-AQ campaign. GCAS was designed to simulate the
726 spectral capabilities of TEMPO and GEMS, but with a much finer pixel resolution of approximately 250 x 560 m at flight
727 altitude (Janz et al., 2019; Lee et al., 2024). GCAS uses a push-broom remote sensing technique and consists of two
728 spectrometer channels: a UV-Vis channel (300-490 nm) optimized for air quality measurements, and a Vis-NIR channel (480-
729 900 nm) for ocean color observations (Kowalewski and Janz, 2014; Lee et al., 2024). This work focuses on the NO₂ retrieval
730 from spectra in the UV-Vis channel. Retrieval details and validation results can be found in Judd et al., (2020) but were
731 previously found to be unbiased with uncertainties within +/-25%. As in previous field campaigns, the aircraft executed a
732 “lawnmower” flight pattern with parallel flight lines spaced 6.3 km apart, providing about 10% overlap between flight lines
733 assuming a flight altitude of 28,000 feet. This flight strategy, combined with the instrument’s 45° field of view, allowed for
734 the generation of gap-free NO₂ column maps up to three times per day, period referred to as a “raster”. Due to the short duration
735 of each raster period (~3 hours), local meteorological conditions often influence the fine-scale structures observed in the GCAS
736 NO₂ data (Goldberg et al., 2024). Here, we evaluate the WRF-Chem runs against GCAS for several flight days: 18 March, 19
737 March, 23 March, and 25 March 2024.
738

739 We perform the evaluation for each raster separately to isolate specific flight patterns and accurately evaluate spatial gradients
740 in NO₂ between the model and observations. For each analysis, GCAS pixels corresponding to the flagged raster were retained



741 for comparison. Additional filters were applied to remove poor-quality retrievals. We masked pixels with cloud or sun glint
742 contamination based on a provided flag variable (`cloud_glint_flag = 1`) and discarded retrievals with missing data or undefined
743 AMFs. GCAS provides separate NO₂ vertical columns above and below the aircraft, as well as model-derived scattering
744 weights, and AMFs for both portions. The above and below aircraft contributions can be approximated as the stratospheric
745 and tropospheric contributions, respectively. For this evaluation, we focus exclusively on the NO₂ column below the aircraft
746 or the tropospheric column NO₂, which is the portion most relevant to surface-level air quality and most comparable to our
747 WRF-Chem results. We compute the below-aircraft averaging kernel, A_i^{below} , as:

$$748 \quad A_i^{below} = \frac{SW_i}{AMF_{below}} \quad (17)$$

749 This averaging kernel represents the satellite-equivalent vertical sensitivity to NO₂ below the aircraft and was used to weigh
750 the WRF-Chem vertical profile.

751
752 WRF-Chem output including, NO₂ mixing ratio, pressure, temperature, and height were used to compute air density and
753 convert volume mixing ratios to number densities as previously done in the GEMS evaluation. Each GCAS pixel was
754 temporally matched to the nearest model output time (rounded to nearest hour) and spatially co-located by finding the nearest
755 WRF-Chem grid cell. To isolate the portion of the model column below the aircraft, we filtered the model levels based on the
756 aircraft altitude reported at each pixel. We compute the tropospheric column as shown in Eq. (10). To generate a model column
757 that reflects the vertical sensitivity of the GCAS retrieval, we interpolate the WRF-Chem profile to the number of GCAS
758 vertical layers (49), converted the mixing ratios to number density, and applied the GCAS averaging kernel to yield WRF-
759 GCAS.

760
761 The maps in Fig. 8 illustrate a spatial comparison between (a) GCAS, (b) WRF-GCAS_{Updated}, and (c) WRF-GCAS_{Base} over
762 BMR for a flight day on 18 March 2024. 18 March represents a typical example of local pollution dominating BMR with
763 minimal influences from long-range pollution transport and biomass burning. The GCAS instrument generally places
764 tropospheric column NO₂ values in BMR between $5 \times 10^{15} - 2 \times 10^{16}$ molecules cm⁻², with the largest enhancements observed
765 in the city center, as also seen in the GEMS data (Fig. 7). A clear N-S plume is visible in the data, reflecting persistent southerly
766 onshore flow from the Gulf of Thailand. This pattern coincides with the seasonal shift from the northeast to southwest
767 monsoon. Overall, WRF-GCAS_{Updated} can generally capture the spatial differences and magnitudes of tropospheric column
768 NO₂ in BMR for different raster periods compared to WRF-GCAS_{Base}. GCAS also illustrates enhanced NO₂ columns southeast
769 of Bangkok in a region known as the Eastern Economic Corridor (EEC), a major hub for industrial activity (e.g., automotive
770 manufacturing, petrochemicals, electronics). WRF_{Updated} and WRF_{Base} tend to underestimate pollution levels in the EEC. This
771 is likely related to wind speed overprediction and a lack of updated regional source data in the EDGAR v5 inventory (since
772 this is a region outside of the performed inversion). Information from a local emissions inventory, or additional inversions

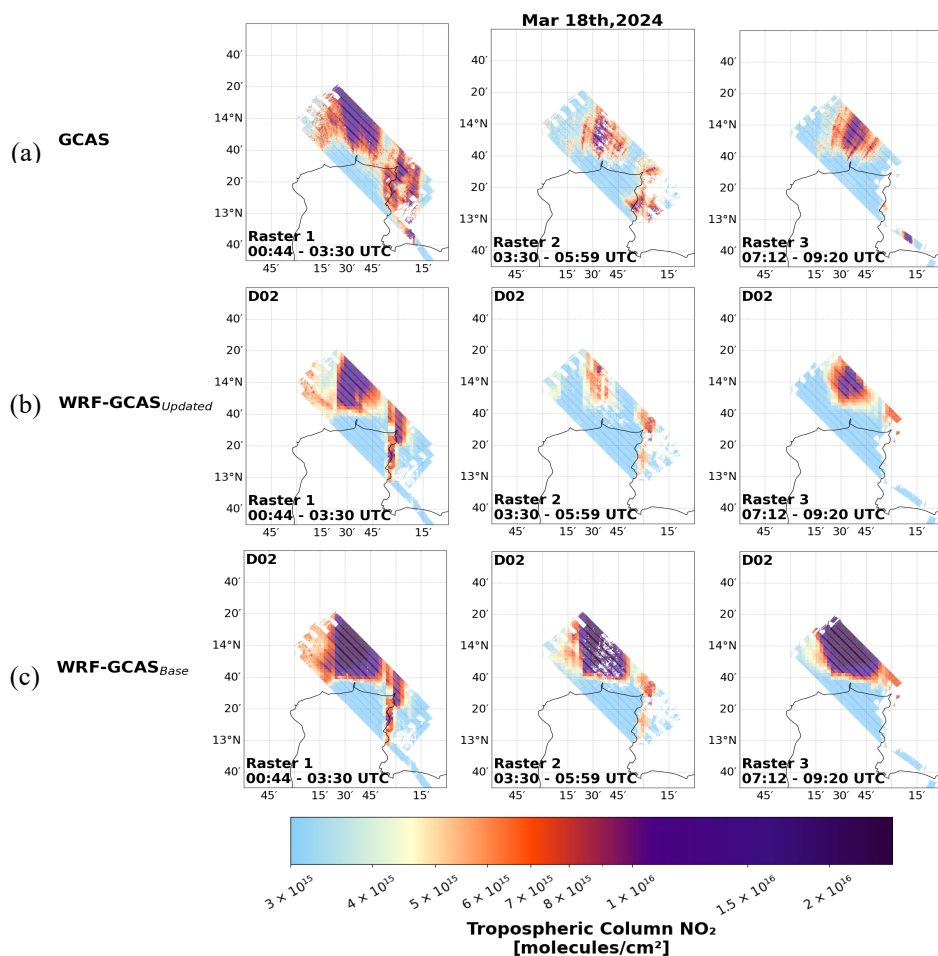


773 performed on this region could aid the model in better representing the air quality in this region, which has similar magnitudes
774 of column NO₂ (2×10^{16} molecules cm⁻²) to the Bangkok city center.

775
776 Statistics for this analysis are shown in Table 2. Overall, statistics are representative of substantial bias and error improvements
777 from WRF_{Base}, which significantly overpredicts column NO₂ amounts in the region for all raster periods. For example, ME
778 and RMSE are improved by ~62% from WRF_{Base}. Mean biases are negative which indicate WRF_{Updated} is underpredicting NO₂
779 columns. This is likely the result of the windspeed overprediction. However, this underprediction is improved throughout the
780 day as seen in Fig. S20a, S20b. This is in opposition to WRF_{Base}, which increases in biases and error for each raster as also
781 shown in Fig. S20a, S20b. These daytime patterns also highlight an important distinction between the benefits of geostationary
782 (GEMS) versus LEO observations. Morning improvements are particularly strong because the inversion directly constrains
783 the rapid rise in emissions during the morning, something that LEO sensors generally under sample due to their limited
784 overpass frequency. Midday and afternoon performance remains improved as well, but the morning hours show the clearest
785 advantage of daytime GEO sampling for capturing short-timescale emission variability.

786
787 Correlations remain high (0.6 – 0.8) for both model cases, however, WRF_{Updated} has weaker correlations likely due to (i) subtle
788 shifts in the urban plume placement (i.e., shift in a more northerly direction), and (ii) a reduction in dynamic range after
789 emissions corrections. For example, when plume magnitudes are lowered, the variability shrinks allowing the correlations to
790 become less sensitive to spatial-temporal agreement and more sensitive to small plume-placement differences as is the case
791 here.

792
793



794

795 **Figure 8.** Spatial comparison over the BMR on 18 March 2024 of tropospheric NO₂ columns from (a) GCAS, (b) WRF-
796 GCAS_{Updated} D02, and (c) WRF-GCAS_{Base} D02 for raster periods corresponding to morning, afternoon, and early evening local
797 time.

798 6.4.2. NO_xO₃ and CANOE (DC-8)

799 We additionally compare the model simulation to in situ NO₂ data gathered by the National Center for Atmospheric Research's
800 (NCAR) NO_xO₃ and NASA's GSFC's Compact Airborne NO₂ Instrument (CANOE) aboard the DC-8 aircraft. The NO_xO₃
801 instrument is a 3-channel chemiluminescence instrument designed for the measurement of NO, NO₂, and O₃ (Ridley et al.,
802 1992; Ridley and Grahek, 1990). CANOE measures NO₂ using non-resonant laser induced fluorescence (LIF) (St. Clair et al.,
803 2019). We use the 1-sec DC-8 data for the flights conducted in Thailand during March 2024 (18 March, 25 March). A visual
804 depiction of the DC-8 flight path is shown in Fig. 17a, 17b. The typical flight path included several low-altitude
805 descents/ascent over several airports (see Fig. 17b) along with long-distance transects across Central Thailand.

806



807 To evaluate model performance, we match hourly WRF-Chem outputs from both the 20 km (D01) and 4 km (D02) domains
808 to the aircraft location and time. For each observation, we extract co-located model NO₂ values along the aircraft track. Profiles
809 are filtered by location (e.g., Don Mueang International Airport in Bangkok) and direction (e.g., ascent or descent) using flags
810 in the provided observational datasets. Individual profiles are grouped by their unique number, and we bin the observations
811 and model output by altitude (50 m vertical bins). For each bin, we compute mean NO₂ from the aircraft and model datasets.
812 These vertically resolved comparisons allow us to assess model skill in capturing the observed structure and magnitude of NO₂
813 within the boundary layer and lower troposphere.

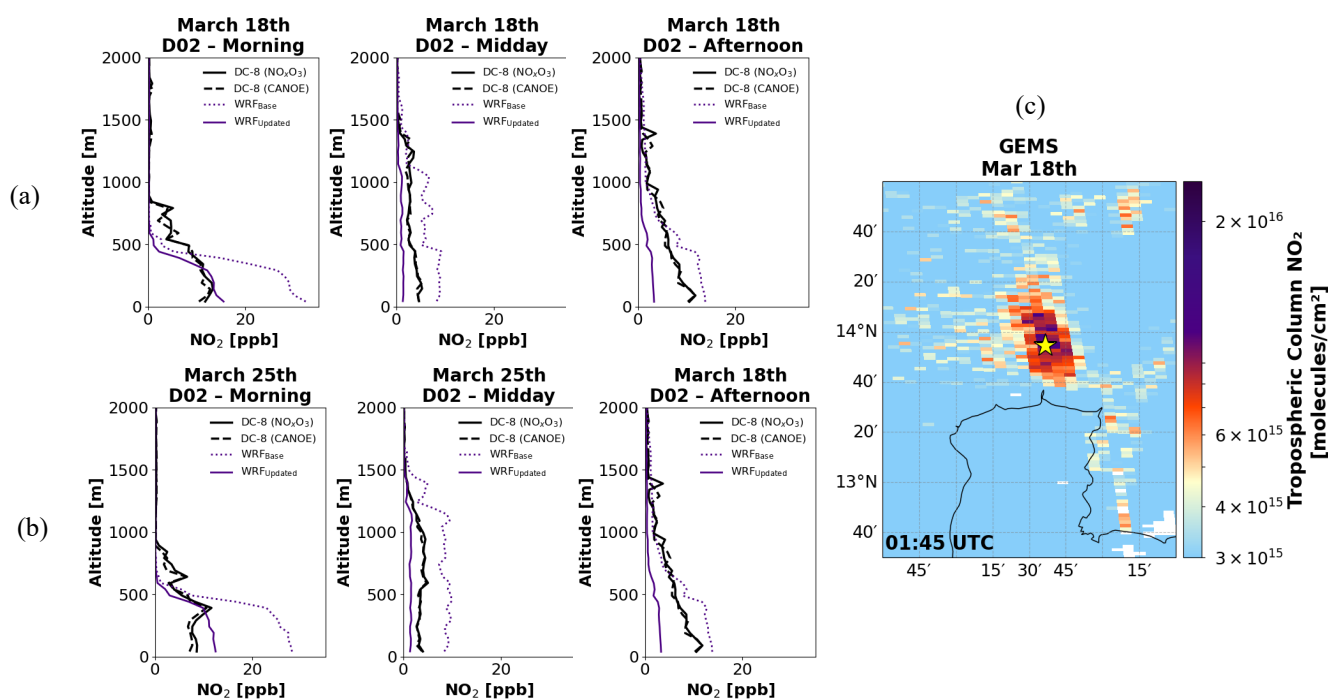
814
815 Figure 9 depicts a comparison of aggregated in situ NO₂ vertical profiles over the Don Mueang International airport for (a) 18
816 March and (b) 25 March. Model scenarios are shown in purple, and in situ information from two instruments aboard the DC-
817 8, NO_xO₃ (solid) and CANOE (dashed) are displayed in black. The location of the Don Mueang International Airport with
818 respect to the Bangkok urban plume is depicted in (c). We separate and group the data by time of day to gauge how the model
819 runs perform with respect to time of day. As shown in Fig. 9, the NO_xO₃ and CANOE NO₂ measurements exhibit excellent
820 agreement throughout the analysis period. This consistency between two independent in situ instruments strengthens
821 confidence in the observational data used for model evaluation. Comparison with DC-8 in situ NO₂ profiles show that WRF_{Base}
822 consistently overestimated observed concentrations, with a mean bias of +1.3 ppb and normalized mean bias near 80%. Figure
823 9a and Figure 9b indicate the overestimation is most pronounced near the surface during the morning, where WRF_{Base} exceeds
824 observations by nearly 25 ppb. In contrast, WRF_{Updated} captures the observed morning surface enhancements accurately. As
825 time progresses, however, WRF_{Updated} begins to underestimate the column (average bias ~ -0.8 ppb), though both mean error
826 and RMSE remain improved relative to WRF_{Base} (Table 2). This daytime behavior likely reflects the nature of the GEMS-
827 based emission constraints, which are directly applied only until 14:00:00 LT, after which a single daily scaling factor is
828 applied on the input emissions. As afternoon PBL growth and photochemistry evolve, the fixed scaling likely results in an
829 underestimation in the afternoon profiles. Additionally, overestimated model winds speeds may further dilute surface
830 concentrations, likely contributing to the midday and afternoon biases shown in WRF_{Updated}.

831
832 Correlations for WRF_{Updated} remain high ($r = 0.93 - 0.97$) indicating the simulation preserved the observed structure while
833 improving the overprediction. Overall, these results highlight the effectiveness of the emission updates in accurately capturing
834 morning surface air quality. This suggests that while the updated emissions substantially improve the magnitude of modelled
835 NO₂, remaining discrepancies are driven primarily by meteorological transport rather than emission magnitude.

836



837



838

839 **Figure 9.** Comparison of WRF-Chem D02 simulations (WRF_{Base}: dotted purple; WRF_{Updated}: solid purple) with airborne in situ
840 measurements from the CANOE (dashed black) and NO_xO₃ (solid black) instruments aboard the DC-8 for (a) 18 March and
841 (b) 25 March 2024. Profiles are grouped by morning (06:00:00–11:00:00 LT), midday (11:00:00–13:00:00 LT), and afternoon
842 (13:00:00–17:00:00 LT) approaches at Don Mueang International Airport in northern Bangkok, whose location relative to the
843 Bangkok urban plume is shown within a GEMS snapshot in (c).
844

845 7 Discussion

846 7.1 Implications of GEMS NO₂ retrieval biases

847 Comparisons between GEMS tropospheric NO₂ columns and independent column references indicate a systematic low bias in
848 the GEMS product, particularly over the Bangkok region. In our analysis during ASIA-AQ, GEMS total NO₂ columns are
849 generally lower than coincident Pandora total column NO₂ observations (Fig. S13) (mean bias $\approx -9.2 \times 10^{15}$ molecules cm⁻²),
850 consistent with recent independent validation studies of the operational GEMS v3 product over Bangkok and South Korea that
851 report low biases relative to ground-based sun-photometer and DOAS measurements (Bae et al., 2025; Jung et al., 2025). Bae
852 et al. (2025) shows that GEMS v3 increasingly underestimates NO₂ relative to Pandora under high-NO₂ conditions ($>1 \times 10^{16}$
853 molecules cm⁻²) as is the case for Bangkok pollution levels. In Jung et al. (2025), validation results over Bangkok indicate a

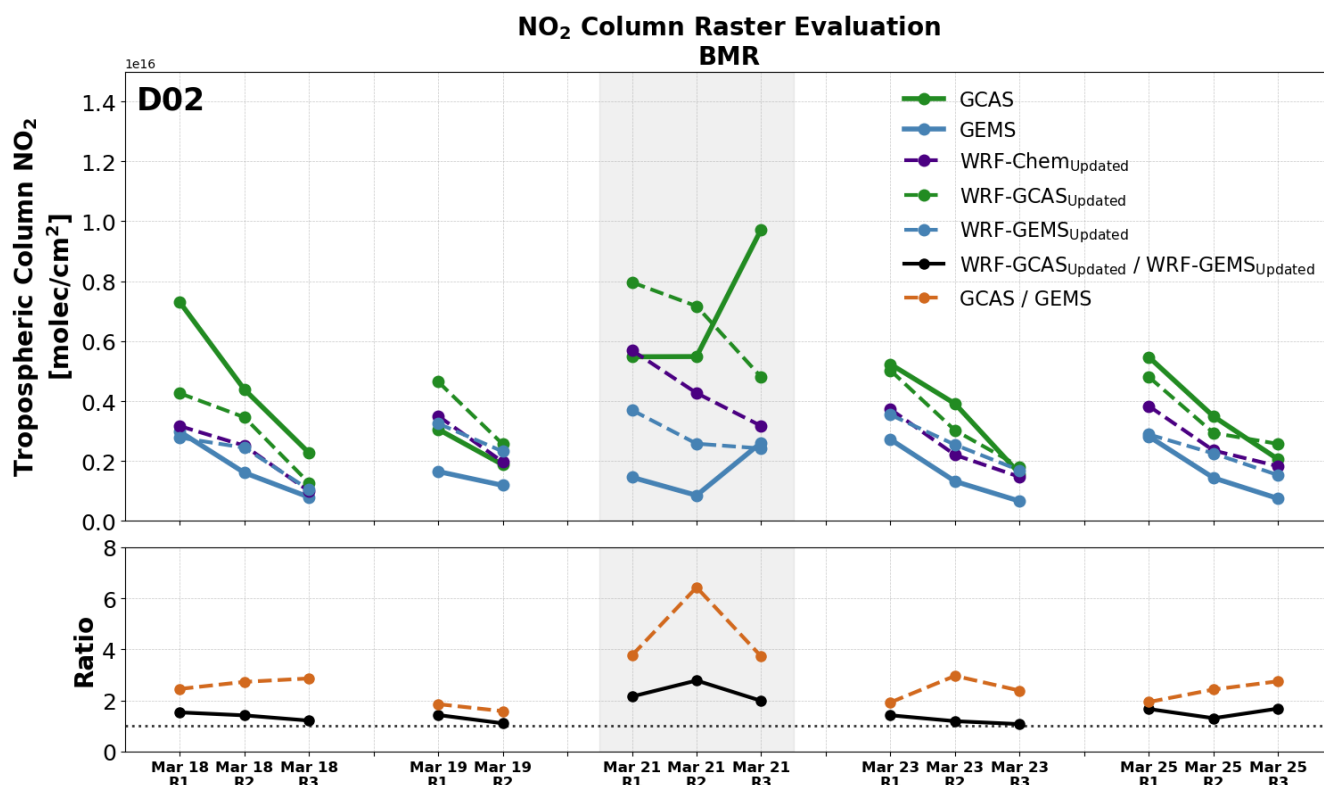


854 pronounced low bias in GEMS tropospheric NO₂ columns relative to Pandora, with regression slopes of ~0.35 for v2.0 and
855 ~0.28 for v3.0, indicating increasing underestimation at higher NO₂ levels. While moderate correlations ($r \approx 0.6-0.7$) suggest
856 that GEMS captures temporal variability, column magnitudes are substantially underestimated, particularly under polluted
857 conditions. The persistence of this behavior in the v3.0 product indicates that the low bias is not fully corrected by recent
858 algorithm updates and is consistent with retrieval sensitivity limitations in highly polluted urban environments (Jung et al.,
859 2025).

860 To further evaluate the relative behavior of GEMS and airborne GCAS NO₂ columns, we compare their tropospheric columns
861 using WRF_{Updated} as a common transfer framework (Fig. 10). Figure 10 compares the observed GCAS/GEMS NO₂ column
862 ratios with ratios calculated after both datasets are mapped through WRF_{Updated}. In the observations, GCAS columns are
863 consistently higher than GEMS, with GCAS/GEMS ratios of ~2–3 on most days and values reaching ~6–7 on 21 March. In
864 contrast, the corresponding WRF-GCAS_{Updated}/WRF-GEMS_{Updated} ratios are substantially smaller (~1.1–1.7), even on 21
865 March. This is consistent with a low bias in GEMS NO₂ columns as found in previous comparisons.

866 In our study, the comparisons with independent aircraft and ground-based observations indicate the satellite-constrained
867 emissions presented here may represent a low estimate. In particular, the systematic low bias in GEMS NO₂ is consistent with
868 the negative biases often seen in the updated simulations. Importantly, this bias could not be diagnosed using the satellite data
869 alone. Here, the integration of ground-based, airborne, satellite, and model data provides a powerful framework not only for
870 improving emissions but also for identifying limitations within individual observing systems. While WRF_{Updated} clearly
871 outperforms the baseline model, the combined observational evidence highlights the necessity of a multi-platform validation
872 to fully interpret the satellite-based emission estimates.

873 Despite this bias, the high-frequency daytime sampling provided by geostationary observations offers critical constraints on
874 daytime variability and plume evolution that are particularly valuable for emission inversion and air quality modelling. For
875 example, the GEMS-constrained emission adjustments presented here were critical for improving the temporal evolution of
876 NO_x in WRF-Chem, resulting in substantial and robust improvements in model performance across independent evaluations.
877 Future work may further benefit from the application of bias-corrected GEMS products or future GEMS algorithm updates
878 and corrections (e.g., v4 products).



879

880

881

882

883

884

885

Figure 10. Daily raster (e.g., R1, R2, R3) comparison of tropospheric NO₂ columns from WRF_{Updated} D02 (dashed purple), WRF-GCAS_{Updated} D02 (dashed green), WRF-GEMS_{Updated} D02 (dashed blue), GCAS (green), and GEMS (blue) for ASIA-AQ flight days. Dashed model lines indicate simulations with instrument-specific averaging kernels applied. The bottom panel illustrates the ratio GCAS/GEMS (orange) and WRF-GCAS/WRF-GEMS (black).

886

8 Conclusion and Discussion

887

8.1 A GEO-constrained framework for anthropogenic NO_x emissions

888

Accurate urban NO_x emissions remain a major challenge for air quality modeling efforts, but geostationary satellites now offer a path forward. This work takes a novel approach in improving urban NO_x emissions using daytime GEO satellite observations.

889

We quantify and reduce biases in modeled NO₂ over the Bangkok Metropolitan Region (BMR), by integrating GEMS constraints into a high-resolution model's daytime prior emission profile. We first used top-down inversions of hourly GEMS

890

NO₂ columns with the Cross-Sectional Flux (CSF) method to develop an average daytime NO_x profile for the BMR in March 2024. Using this information, we developed and applied an optimization framework that incorporates physical constraints (i.e.,

891

892

893



894 with regards to emissions accumulation and lifetime) to reshape the WRF-Chem's daytime emission pattern and magnitude to
895 better reflect observed emissions variability in the BMR.

896

897 This represents one of the first applications of the *ddeg* framework to estimate hourly urban NO_x emissions with geostationary
898 observations in Southeast Asia. In contrast to a full chemical reanalysis, the *ddeg*-based framework provides an efficient and
899 scalable alternative that does not require repeated model reinitialization of extensive chemical state optimization. This makes
900 the approach particularly suitable for regional applications and for broader application across different modeling systems and
901 urban environments within the domain of GEO sensors.

902

903 **8.2 Model improvements across independent observational platforms**

904 Re-running WRF-Chem (D01 – 20 km; D02 – 4 km) with an updated NO_x emission profile (WRF_{Updated}) led to substantial
905 improvements across multiple independent datasets. Model evaluation with ground monitors, Pandora, GCAS, and DC-8
906 observations consistently showed reduced biases and errors relative to the baseline simulation based on EDHAR v5 emissions.
907 For example, surface-level comparisons with Thailand PCD ground network data confirmed some of these trends in
908 WRF_{Updated}, with mean biases in NO₂ and NO_x decreasing from +12 - +14 ppbV in WRF_{Base} to roughly -3 ppbV in WRF_{Updated}.
909 At the Bangkok Pandora site, mean bias shifted from strongly positive ($+7.9 \times 10^{15}$ molecules cm⁻²) to negative, and normalized
910 mean errors decreased by ~20-25%. Evaluation against GCAS airborne column retrievals further showed that the emissions
911 updates improved spatial variability and magnitude of NO₂ across the Bangkok urban plume, reducing mean and root mean
912 square errors by ~60% compared to WRF_{Base}. The DC-8 in situ vertical profiles further illustrated that WRF_{Updated} could
913 substantially reduce near-surface overestimation in morning hours and preserve the observed vertical structure of NO₂ mixing
914 ratios.

915

916 **8.3 Assessing GEMS bias through multi-platform integration**

917 Overall, these results demonstrate that incorporating geostationary satellite constraints into regional, high-resolution (4 km)
918 chemical transport models can substantially improve the representation of urban air quality over Bangkok. Large biases in the
919 baseline simulation are likely driven by reliance on outdated global emissions inventories (e.g., EDGAR v5), which do not
920 reflect recent changes in regional anthropogenic activity, as well as uncertainties in bottom-up methodologies where updated
921 local estimates appear systematically high. The satellite-constrained emission estimates derived here are consistent with
922 independent top-down approaches (e.g., TCR-3) based on different satellite platforms and methodologies, increasing
923 confidence in the inferred reductions.



924 Comparisons with independent aircraft and ground-based observations further indicate that the GEMS-constrained emissions
925 presented here may represent an underestimate. In particular, the systematic low bias reported for the GEMS v3 NO₂ product
926 is consistent with the remaining negative biases observed in WRF_{Updated}. This bias could not be diagnosed using the satellite
927 data alone. Instead, the integration of ground-based, airborne, satellite and model information together provides a powerful
928 framework not only for improving emission estimations, but also for identifying limitations within individual observing
929 systems.

930 **8.4 Value of hourly GEO constraints, high-resolution modelling and future directions**

931 A key strength of this framework is the use of hourly daytime constraints uniquely provided by geostationary observations,
932 which enable direct characterization of daytime emission variability and plume evolution that cannot be captured by once-
933 daily low-Earth-orbit measurements. These daytime constraints are particularly important for urban environments, where
934 emissions, chemistry, and boundary-layer dynamics vary rapidly and strongly influence air quality impacts.

935 Coarse (~12 km) simulations have been shown to inadequately represent circulations in coastal environments, and nonlinear
936 NO_x chemistry, leading to systematic biases in simulations of NO₂ (Hsu et al., 2026; Valin et al., 2011; Verreyken et al., 2025;
937 Yu et al., 2023). These limitations in model resolution are expected in coastal megacities such as Bangkok with complex local
938 topography and land-sea contrasts. Consistent with recent TEMPO-based emission studies indicating that model resolution
939 can limit the robustness of GEO-based top-down NO_x constraints (Hsu et al., 2026), these considerations motivate the use of
940 4 km WRF-Chem simulations in this work as a necessary framework for accurately interpreting geostationary satellite
941 observations and constraining urban NO_x emissions.

942 While remaining discrepancies, including the negative model biases, are likely influenced in part by overpredicted model wind
943 speeds and associated transport errors, future work could benefit from finer-resolution simulations (< 4 km) and more
944 advanced urban parameterizations (e.g., multi-layer urban canopy models; Liu et al., (2025)) to better represent urban flow,
945 drag, and mixing. Continued validation and further development of bias-corrected for updated GEMS retrievals will also
946 strengthen the use of geostationary NO₂ products. Nevertheless, the high-frequency daytime sampling provided by GEMS
947 already offers critical information for emission inversion, and the integration of GEMS-derived constraints into WRF-Chem
948 represents a scalable pathway toward near-real-time, satellite-informed emissions estimation and improved air quality
949 forecasting for rapidly developing megacities.



950 **Code Availability.**

951 The code repository for *ddeq v1* is available on GitLab: <https://gitlab.com/empa503/remote-sensing/ddeq>, Kuhlmann, 2024a.
952 The implementation of *ddeq v1* for top-down NO_x estimates and model optimization scripts are publicly available via Zenodo
953 (<https://doi.org/10.5281/zenodo.18381169>).

954 **Data Availability.**

955 All ASIA-AQ field campaign data used in this study (i.e., GEMS NO₂ v3, NO_{xy}O₃, CANOE, GCAS, Thailand PCD air quality
956 monitoring data) are openly available and were acquired from their NASA Langley Research Center maintained archive:
957 <https://www-air.larc.nasa.gov/cgi-bin/ArcView/asiaaq>. Pandora total column NO₂ observations are available through the
958 Pandonia Global Network website: <https://www.pandonia-global-network.org/home/documents/pgn-data/>. ERA5
959 meteorological reanalysis data were obtained from the Copernicus Climate Data Store: <https://cds.climate.copernicus.eu/>.
960 Global emissions used in this study are openly available as well, HTAP v3.2 (https://edgar.jrc.ec.europa.eu/dataset_htap_v32),
961 MIXv3.1 (<https://csl.noaa.gov/groups/csl4/modeldata/data/Li2023/>), EDGARv5 (https://edgar.jrc.ec.europa.eu/dataset_ghg50),
962 ODIAC (<https://db.cger.nies.go.jp/dataset/ODIAC/>). THAI-KMUTT, and TCR-3 emissions can be made available upon
963 request.

964 **Supplement.**

965 The supplement related to this article is available online.

966 **Author Contributions**

967 JAC designed the study, performed the model simulations, conducted the data analysis, prepared all figures, and wrote the
968 initial draft of the manuscript. PS supervised the project, contributed ideas, guidance, and discussions regarding the model



969 framework and interpretation of results. MM provided additional guidance on the modeling framework and interpretation of
970 results. All authors discussed the results and contributed to the final version of the manuscript.

971 **Competing Interests**

972 At least one of the (co-)authors is a member of the editorial board of Atmospheric Chemistry and Physics.

973 **Acknowledgements**

974 We thank the entire ASIA-AQ team for their contributions to the field experiment. We extend our gratitude to the instrument
975 teams for their efforts in conducting in situ measurements, to the airborne remote sensing teams (HSRL-2 and GCAS) for their
976 data collection and support, and the GEMS team for providing the data utilized in this work. The TCR-3 product was generated
977 by calculations using the Earth Simulator with the support of the Japan Agency for Marine-Earth Science and Technology.

978 **Financial Support**

979 The funding for this research came from the National Aeronautics and Space Administration under awards 80NSSC22M0266
980 and 80NSSC23K0786. The views expressed in this manuscript are those of the authors and do not reflect the views of NASA.

981 **References**

982
983 Agarwal, P., Stevenson, D. S., and Heal, M. R.: Evaluation of WRF-Chem-simulated meteorology and aerosols over northern
984 India during the severe pollution episode of 2016, *Atmospheric Chemistry and Physics*, 24, 2239–2266,
985 <https://doi.org/10.5194/acp-24-2239-2024>, 2024.

986 Ahmadov, R., McKeen, S. A., Robinson, A. L., Bahreini, R., Middlebrook, A. M., Gouw, J. A. de, Meagher, J., Hsie, E.-Y.,
987 Edgerton, E., Shaw, S., and Trainer, M.: A volatility basis set model for summertime secondary organic aerosols over the
988 eastern United States in 2006, <https://doi.org/10.1029/2011JD016831>, 2012.

989 Anav, A., Sorrentino, B., Collalti, A., Paoletti, E., Sicard, P., Coulibaly, F., Manzini, J., Hoshika, Y., and De Marco, A.:
990 Meteorological, chemical and biological evaluation of the coupled chemistry-climate WRF-Chem model from regional to



- 991 urban scale. An impact-oriented application for human health, *Environmental Research*, 257, 119401,
992 <https://doi.org/10.1016/j.envres.2024.119401>, 2024.
- 993 Anenberg, S. C., Mohegh, A., Goldberg, D. L., Kerr, G. H., Brauer, M., Burkart, K., Hystad, P., Larkin, A., Wozniak, S., and
994 Lamsal, L.: Long-term trends in urban NO₂ concentrations and associated paediatric asthma incidence: estimates from global
995 datasets, *The Lancet Planetary Health*, 6, e49–e58, [https://doi.org/10.1016/S2542-5196\(21\)00255-2](https://doi.org/10.1016/S2542-5196(21)00255-2), 2022.
- 996 ASIA-AQ White Paper | ASIA-AQ: https://espo.nasa.gov/asia-aq/document/ASIA-AQ_White_Paper, last access: 6 January
997 2025.
- 998 `minimize(method='SLSQP')` — SciPy v1.16.2 Manual: [https://docs.scipy.org/doc/scipy/reference/optimize.minimize-](https://docs.scipy.org/doc/scipy/reference/optimize.minimize-slsqp.html)
999 `slsqp.html`, last access: 4 November 2025.
- 1000 Aung, S. H., Gheewala, S. H., Winijkul, E., Panyametheekul, S., and Prapasongsa, T.: Environmental impacts and costs of
1001 ozone formation in Bangkok Metropolitan Region, *Atmospheric Pollution Research*, 16, 102450,
1002 <https://doi.org/10.1016/j.apr.2025.102450>, 2025.
- 1003 Bae, K., Richter, A., Lange, K., Friedrich, M. M., Pinardi, G., Roozendaal, M. V., Merlaud, A., Fayt, C., Bösch, T., Zilker, B.,
1004 Latsch, M., Behrens, L. K., Lee, H., Jung, Y., Hong, H., Chang, L.-S., and Song, C.-K.: Comparison of GEMS v3.0
1005 tropospheric NO₂ columns with ground-based DOAS instruments in Ulsan, *GIScience & Remote Sensing*, 2025.
- 1006 Beirle, S., Boersma, K. F., Platt, U., Lawrence, M. G., and Wagner, T.: Megacity Emissions and Lifetimes of Nitrogen Oxides
1007 Probed from Space, *Science*, 333, 1737–1739, <https://doi.org/10.1126/science.1207824>, 2011.
- 1008 Bond, T. C., Streets, D. G., Yarber, K. F., Nelson, S. M., Woo, J.-H., and Klimont, Z.: A technology-based global inventory
1009 of black and organic carbon emissions from combustion, <https://doi.org/10.1029/2003JD003697>, 2004.
- 1010 Bond, T. C., Bhardwaj, E., Dong, R., Jogani, R., Jung, S., Roden, C., Streets, D. G., and Trautmann, N. M.: Historical emissions
1011 of black and organic carbon aerosol from energy-related combustion, 1850–2000, *Global Biogeochemical Cycles*, 21,
1012 <https://doi.org/10.1029/2006GB002840>, 2007.
- 1013 Chen, F. and Chen, Z.: Cost of economic growth: Air pollution and health expenditure, *Science of The Total Environment*,
1014 755, 142543, <https://doi.org/10.1016/j.scitotenv.2020.142543>, 2021.
- 1015 Cho, C., Franchin, A., Flocke, F., Lesko, K., Owen, C., Hall, S. R., Ullmann, K., Apel, E. C., Hills, A. J., Hornbrook, R. S.,
1016 Roozitalab, B., Jeong, D., Diskin, G. S., Choi, Y., DiGangi, J. P., Miech, J., Wolfe, G. M., Hanisco, T. F., St. Clair, J. M.,
1017 Liao, J., Delaria, E. R., Sebol, A., Hannun, R. A., Wennberg, P. O., Ball, K., Lee, Y. R., Huey, L. G., Tanner, D. J., Arterburn,



- 1018 L., Blake, D. R., Blake, N. J., Barletta, B., Meinardi, S., Min, K.-E., Kang, H., Nam, W., Wisthaler, A., Piel, F., Wojnowski,
1019 W., Dibb, J., and Crawford, J.: Insights on Ozone Formation Sensitivity in Southeast and East Asian Megacities during ASIA-
1020 AQ, *EGUsphere*, 1–29, <https://doi.org/10.5194/egusphere-2025-6434>, 2026.
- 1021 Choi, S., Lamsal, L. N., Follette-Cook, M., Joiner, J., Krotkov, N. A., Swartz, W. H., Pickering, K. E., Loughner, C. P., Appel,
1022 W., Pfister, G., Saide, P. E., Cohen, R. C., Weinheimer, A. J., and Herman, J. R.: Assessment of NO₂ observations during
1023 DISCOVER-AQ and KORUS-AQ field campaigns, *Atmospheric Measurement Techniques*, 13, 2523–2546,
1024 <https://doi.org/10.5194/amt-13-2523-2020>, 2020.
- 1025 Christopoulos, J. A., Saide, P. E., Ferrare, R., Collister, B., Barton-Grimley, R. A., Scarino, A. J., Collins, J., Hair, J. W., and
1026 Nehrir, A.: Improving Planetary Boundary Layer Height Estimation From Airborne Lidar Instruments, *Journal of Geophysical*
1027 *Research: Atmospheres*, 130, e2024JD042538, <https://doi.org/10.1029/2024JD042538>, 2025.
- 1028 Christopoulos, J.: GEMS Top-Down NO_x Emissions and Model Optimization, Zenodo,
1029 <https://doi.org/10.5281/zenodo.18381169>, 2026.
- 1030
- 1031 Commerce, N. C. for E. P. W. S. S. D. of: NCEP FNL Operational Model Global Tropospheric Analyses, continuing from
1032 July 1999, <https://doi.org/10.5065/D6M043C6>, 2000.
- 1033 Crippa, M., Solazzo, E., Huang, G., Guizzardi, D., Koffi, E., Muntean, M., Schieberle, C., Friedrich, R., and Janssens-
1034 Maenhout, G.: High resolution temporal profiles in the Emissions Database for Global Atmospheric Research, *Sci Data*, 7,
1035 121, <https://doi.org/10.1038/s41597-020-0462-2>, 2020.
- 1036 Elguindi, N., Granier, C., Stavrakou, T., Darras, S., Bauwens, M., Cao, H., Chen, C., Denier van der Gon, H. a. C., Dubovik,
1037 O., Fu, T. M., Henze, D. K., Jiang, Z., Keita, S., Kuenen, J. J. P., Kurokawa, J., Liousse, C., Miyazaki, K., Müller, J.-F., Qu,
1038 Z., Solmon, F., and Zheng, B.: Intercomparison of Magnitudes and Trends in Anthropogenic Surface Emissions From Bottom-
1039 Up Inventories, Top-Down Estimates, and Emission Scenarios, *Earth's Future*, 8, e2020EF001520,
1040 <https://doi.org/10.1029/2020EF001520>, 2020.
- 1041 de Foy, B. and Schauer, J. J.: An improved understanding of NO_x emissions in South Asian megacities using TROPOMI NO₂
1042 retrievals, *Environ. Res. Lett.*, 17, 024006, <https://doi.org/10.1088/1748-9326/ac48b4>, 2022.
- 1043 Fuller, R., Landrigan, P. J., Balakrishnan, K., Bathan, G., Bose-O'Reilly, S., Brauer, M., Caravanos, J., Chiles, T., Cohen, A.,
1044 Corra, L., Cropper, M., Ferraro, G., Hanna, J., Hanrahan, D., Hu, H., Hunter, D., Janata, G., Kupka, R., Lanphear, B., Lichtveld,
1045 M., Martin, K., Mustapha, A., Sanchez-Triana, E., Sandilya, K., Schaeffli, L., Shaw, J., Seddon, J., Suk, W., Téllez-Rojo, M.



- 1046 M., and Yan, C.: Pollution and health: a progress update, *The Lancet Planetary Health*, 6, e535–e547,
1047 [https://doi.org/10.1016/S2542-5196\(22\)00090-0](https://doi.org/10.1016/S2542-5196(22)00090-0), 2022.
- 1048 Gao, Z. and Zhou, X.: A review of the CAMx, CMAQ, WRF-Chem and NAQPMS models: Application, evaluation and
1049 uncertainty factors, *Environmental Pollution*, 343, 123183, <https://doi.org/10.1016/j.envpol.2023.123183>, 2024.
- 1050 Georgoulias, A. K., van der A, R. J., Stammes, P., Boersma, K. F., and Eskes, H. J.: Trends and trend reversal detection in 2
1051 decades of tropospheric NO₂ satellite observations, *Atmospheric Chemistry and Physics*, 19, 6269–6294,
1052 <https://doi.org/10.5194/acp-19-6269-2019>, 2019.
- 1053 Goldberg, D. L., Lamsal, L. N., Loughner, C. P., Swartz, W. H., Lu, Z., and Streets, D. G.: A high-resolution and
1054 observationally constrained OMI NO₂ satellite retrieval, *Atmospheric Chemistry and Physics*, 17, 11403–11421,
1055 <https://doi.org/10.5194/acp-17-11403-2017>, 2017.
- 1056 Goldberg, D. L., Saide, P. E., Lamsal, L. N., de Foy, B., Lu, Z., Woo, J.-H., Kim, Y., Kim, J., Gao, M., Carmichael, G., and
1057 Streets, D. G.: A top-down assessment using OMI NO₂ suggests an underestimate in the NO_x emissions inventory in Seoul,
1058 South Korea, during KORUS-AQ, *Atmospheric Chemistry and Physics*, 19, 1801–1818, [https://doi.org/10.5194/acp-19-1801-](https://doi.org/10.5194/acp-19-1801-2019)
1059 2019, 2019.
- 1060 Goldberg, D. L., Tao, M., Kerr, G. H., Ma, S., Tong, D. Q., Fiore, A. M., Dickens, A. F., Adelman, Z. E., and Anenberg, S.
1061 C.: Evaluating the spatial patterns of U.S. urban NO_x emissions using TROPOMI NO₂, *Remote Sensing of Environment*, 300,
1062 113917, <https://doi.org/10.1016/j.rse.2023.113917>, 2024.
- 1063 Gong, S. L., Barrie, L. A., and Blanchet, J.-P.: Modeling sea-salt aerosols in the atmosphere: 1. Model development, *Journal*
1064 *of Geophysical Research: Atmospheres*, 102, 3805–3818, <https://doi.org/10.1029/96JD02953>, 1997.
- 1065 Graziosi, F. and Manca, G.: Quantification of Hotspot Methane Emissions Using Sentinel-5P TROPOMI Observations, *JRC*
1066 *Publications Repository*, <https://doi.org/10.2760/4473858>, 2025.
- 1067 Grell, G., Freitas, S. R., Stuefer, M., and Fast, J.: Inclusion of biomass burning in WRF-Chem: impact of wildfires on weather
1068 forecasts, *Atmospheric Chemistry and Physics*, 11, 5289–5303, <https://doi.org/10.5194/acp-11-5289-2011>, 2011.
- 1069 Guenther, A., Karl, T., Harley, P., Wiedinmyer, C., Palmer, P. I., and Geron, C.: Estimates of global terrestrial isoprene
1070 emissions using MEGAN (Model of Emissions of Gases and Aerosols from Nature), *Atmospheric Chemistry and Physics*, 6,
1071 3181–3210, <https://doi.org/10.5194/acp-6-3181-2006>, 2006.



- 1072 Guizzardi, D., Crippa, M., Butler, T., Keating, T., Wu, R., Kaminski, J., Kuenen, J., Kurokawa, J., Chatani, S., Morikawa, T.,
1073 Pouliot, G., Racine, J., Moran, M. D., Klimont, Z., Manseau, P. M., Mashayekhi, R., Henderson, B. H., Smith, S. J., Hoesly,
1074 R., Muntean, M., Banja, M., Schaaf, E., Pagani, F., Woo, J.-H., Kim, J., Pisoni, E., Zhang, J., Niemi, D., Sassi, M., Duhamel,
1075 A., Ansari, T., Foley, K., Geng, G., Chen, Y., and Zhang, Q.: The HTAP_v3.2 emission mosaic: merging regional and global
1076 monthly emissions (2000–2020) to support air quality modelling and policies, *Earth System Science Data*, 17, 5915–5950,
1077 <https://doi.org/10.5194/essd-17-5915-2025>, 2025.
- 1078 Gulde, S. T., Kolm, M. G., Smith, D. J., Maurer, R., Courrèges-Lacoste, G. B., Sallusti, M., and Bagnasco, G.: Sentinel 4: a
1079 geostationary imaging UVN spectrometer for air quality monitoring: status of design, performance and development, in:
1080 International Conference on Space Optics — ICSO 2014, International Conference on Space Optics — ICSO 2014, 1158–
1081 1166, <https://doi.org/10.1117/12.2304099>, 2017.
- 1082 Hakkarainen, J., Nurmela, J., and Lindqvist, H.: D4.4 Benchmarking of plume detection and quantification methods, 2023.
- 1083 Hakkarainen, J., Kuhlmann, G., Koene, E., Santaren, D., Meier, S., Krol, M. C., van Stratum, B. J. H., Ialongo, I., Chevallier,
1084 F., Tamminen, J., Brunner, D., and Broquet, G.: Analyzing nitrogen dioxide to nitrogen oxide scaling factors for data-driven
1085 satellite-based emission estimation methods: A case study of Matimba/Medupi power stations in South Africa, *Atmospheric
1086 Pollution Research*, 15, 102171, <https://doi.org/10.1016/j.apr.2024.102171>, 2024.
- 1087 Hoesly, R. M., Smith, S. J., Feng, L., Klimont, Z., Janssens-Maenhout, G., Pitkanen, T., Seibert, J. J., Vu, L., Andres, R. J.,
1088 Bolt, R. M., Bond, T. C., Dawidowski, L., Kholod, N., Kurokawa, J., Li, M., Liu, L., Lu, Z., Moura, M. C. P., O'Rourke, P.
1089 R., and Zhang, Q.: Historical (1750–2014) anthropogenic emissions of reactive gases and aerosols from the Community
1090 Emissions Data System (CEDS), *Geoscientific Model Development*, 11, 369–408, <https://doi.org/10.5194/gmd-11-369-2018>,
1091 2018.
- 1092 Hsu, C.-H., Henze, D. K., Mizzi, A. P., Harkins, C., Lyu, C., Cooper, O. R., Schwantes, R. H., He, J., Li, M., Wang, S.,
1093 Stockwell, C. E., Warneke, C., Rollins, A. W., Waxman, E. M., Zuraski, K., Peischl, J., Kondragunta, S., Li, F., Xu, C., Pierce,
1094 R. B., Abad, G. G., Nowlan, C. R., Liu, X., and McDonald, B. C.: Top-Down Estimates of U.S. NO_x Emissions Using TEMPO
1095 and TROPOMI NO₂ Remote Sensing Observations With WRF-Chem/Chem-DART, *Journal of Geophysical Research:
1096 Atmospheres*, 131, e2025JD044223, <https://doi.org/10.1029/2025JD044223>, 2026.
- 1097 Inness, A., Ades, M., Agustí-Panareda, A., Barré, J., Benedictow, A., Blechschmidt, A.-M., Dominguez, J. J., Engelen, R.,
1098 Eskes, H., Flemming, J., Huijnen, V., Jones, L., Kipling, Z., Massart, S., Parrington, M., Peuch, V.-H., Razinger, M., Remy,
1099 S., Schulz, M., and Suttie, M.: The CAMS reanalysis of atmospheric composition, *Atmospheric Chemistry and Physics*, 19,
1100 3515–3556, <https://doi.org/10.5194/acp-19-3515-2019>, 2019.



- 1101 Janz, S. J., Kowalewski, M., Lamsal, L., Nowlan, C., and Judd, L.: Airborne hyperspectral trace gas sensors as testbeds for
1102 geostationary air quality missions, in: Sensors, Systems, and Next-Generation Satellites XXIII, Sensors, Systems, and Next-
1103 Generation Satellites XXIII, 509–518, <https://doi.org/10.1117/12.2533765>, 2019.
- 1104 Jiawei Zhuang, raphael dussin, David Huard, Pascal Bourgault, Anderson Banihirwe, Stephane Raynaud, Brewster Malevich,
1105 Martin Schupfner, Filipe, Charles Gauthier, Sam Levang, André Jüling, Mattia Almansi, RichardScottOZ, RondeauG, Stephan
1106 Rasp, Trevor James Smith, Ben Mares, Jemma Stachelek, Matthew Plough, Pierre, Ray Bell, Romain Caneill, and Xianxiang
1107 Li: pangeo-data/xESMF: v0.8.10, , <https://doi.org/10.5281/ZENODO.4294774>, 2025.
- 1108 Judd, L. M., Al-Saadi, J. A., Szykman, J. J., Valin, L. C., Janz, S. J., Kowalewski, M. G., Eskes, H. J., Veeffkind, J. P., Cede,
1109 A., Mueller, M., Gebetsberger, M., Swap, R., Pierce, R. B., Nowlan, C. R., Abad, G. G., Nehrir, A., and Williams, D.:
1110 Evaluating Sentinel-5P TROPOMI tropospheric NO₂ column densities with airborne and Pandora spectrometers near New
1111 York City and Long Island Sound, Atmospheric Measurement Techniques, 13, 6113–6140, [https://doi.org/10.5194/amt-13-](https://doi.org/10.5194/amt-13-6113-2020)
1112 [6113-2020](https://doi.org/10.5194/amt-13-6113-2020), 2020.
- 1113 Jung, Y., Park, J., Hong, H., Lee, H., and Jeong, U.: Evaluation of GEMS NO Retrieval Algorithm Version 2.0 and 3.0 Using
1114 TROPOMI and Pandora Observations, Korean Journal of Remote Sensing, 41, 803–811,
1115 <https://doi.org/10.7780/kjrs.2025.41.5.8>, 2025.
- 1116 Kim, J., Jeong, U., Ahn, M.-H., Kim, J. H., Park, R. J., Lee, H., Song, C. H., Choi, Y.-S., Lee, K.-H., Yoo, J.-M., Jeong, M.-
1117 J., Park, S. K., Lee, K.-M., Song, C.-K., Kim, S.-W., Kim, Y. J., Kim, S.-W., Kim, M., Go, S., Liu, X., Chance, K., Miller, C.
1118 C., Al-Saadi, J., Veihelmann, B., Bhartia, P. K., Torres, O., Abad, G. G., Haffner, D. P., Ko, D. H., Lee, S. H., Woo, J.-H.,
1119 Chong, H., Park, S. S., Nicks, D., Choi, W. J., Moon, K.-J., Cho, A., Yoon, J., Kim, S., Hong, H., Lee, K., Lee, H., Lee, S.,
1120 Choi, M., Veeffkind, P., Levelt, P. F., Edwards, D. P., Kang, M., Eo, M., Bak, J., Baek, K., Kwon, H.-A., Yang, J., Park, J.,
1121 Han, K. M., Kim, B.-R., Shin, H.-W., Choi, H., Lee, E., Chong, J., Cha, Y., Koo, J.-H., Irie, H., Hayashida, S., Kasai, Y.,
1122 Kanaya, Y., Liu, C., Lin, J., Crawford, J. H., Carmichael, G. R., Newchurch, M. J., Lefer, B. L., Herman, J. R., Swap, R. J.,
1123 Lau, A. K. H., Kurosu, T. P., Jaross, G., Ahlers, B., Dobber, M., McElroy, C. T., and Choi, Y.: New Era of Air Quality
1124 Monitoring from Space: Geostationary Environment Monitoring Spectrometer (GEMS), [https://doi.org/10.1175/BAMS-D-18-](https://doi.org/10.1175/BAMS-D-18-0013.1)
1125 [0013.1](https://doi.org/10.1175/BAMS-D-18-0013.1), 2020.
- 1126 Koster, R. D., Darnenov, A. S., and da Silva, A. M.: The Quick Fire Emissions Dataset (QFED): Documentation of Versions
1127 2.1, 2.2 and 2.4: Technical Report Series on Global Modeling and Data Assimilation - Volume 38, 2015.
- 1128 Kowalewski, M. G. and Janz, S. J.: Remote sensing capabilities of the GeoCAPE Airborne Simulator, in: Earth Observing
1129 Systems XIX, Earth Observing Systems XIX, 496–507, <https://doi.org/10.1117/12.2062058>, 2014.



- 1130 Kuhlmann, G., Koene, E., Meier, S., Santaren, D., Broquet, G., Chevallier, F., Hakkarainen, J., Nurmela, J., Amorós, L.,
1131 Tamminen, J., and Brunner, D.: The *ddeg* Python library for point source quantification from remote sensing images (version
1132 1.0), Geoscientific Model Development, 17, 4773–4789, <https://doi.org/10.5194/gmd-17-4773-2024>, 2024.
- 1133 Kumar, R., Naja, M., Pfister, G. G., Barth, M. C., Wiedinmyer, C., and Brasseur, G. P.: Simulations over South Asia using the
1134 Weather Research and Forecasting model with Chemistry (WRF-Chem): chemistry evaluation and initial results, Geoscientific
1135 Model Development, 5, 619–648, <https://doi.org/10.5194/gmd-5-619-2012>, 2012.
- 1136 Kurokawa, J. and Ohara, T.: Long-term historical trends in air pollutant emissions in Asia: Regional Emission inventory in
1137 ASia (REAS) version 3, Atmospheric Chemistry and Physics, 20, 12761–12793, <https://doi.org/10.5194/acp-20-12761-2020>,
1138 2020.
- 1139 Lee, S., Bae, K., Janz, S. J., Judd, L. M., Xiong, S., Boehmler, J., Jung, Y., Lee, H.-J., Hong, H., Chang, L.-S., Kang, M., Ahn,
1140 M.-H., Song, C.-K., and Park, S. S.: Sensitivity analysis of NO₂ differential slant column density according to spatial resolution
1141 using GCAS data from the SIJAQ 2022 campaign, Atmospheric Environment, 335, 120723,
1142 <https://doi.org/10.1016/j.atmosenv.2024.120723>, 2024.
- 1143 Lennartson, E. M., Wang, J., Gu, J., Castro Garcia, L., Ge, C., Gao, M., Choi, M., Saide, P. E., Carmichael, G. R., Kim, J., and
1144 Janz, S. J.: Diurnal variation of aerosol optical depth and PM_{2.5} in South Korea: a synthesis from AERONET, satellite (GOCI),
1145 KORUS-AQ observation, and the WRF-Chem model, Atmospheric Chemistry and Physics, 18, 15125–15144,
1146 <https://doi.org/10.5194/acp-18-15125-2018>, 2018.
- 1147 Li, M., Kurokawa, J., Zhang, Q., Woo, J.-H., Morikawa, T., Chatani, S., Lu, Z., Song, Y., Geng, G., Hu, H., Kim, J., Cooper,
1148 O. R., and McDonald, B. C.: MIXv2: a long-term mosaic emission inventory for Asia (2010–2017), Atmospheric Chemistry
1149 and Physics, 24, 3925–3952, <https://doi.org/10.5194/acp-24-3925-2024>, 2024.
- 1150 Liu, J., Gao, H., Jia, R., Wang, R., Han, D., Liu, L., Xu, X., and Qiao, Z.: A downscaling framework with WRF-UCM and
1151 LES/RANS models for urban microclimate simulation strategy: Validation through both measurement and mechanism model,
1152 Building and Environment, 269, 112361, <https://doi.org/10.1016/j.buildenv.2024.112361>, 2025.
- 1153 Makkwao, K. and Prueksasit, T.: PM₁₀ Concentration Emitted from Blasting and Crushing Processes of Limestone Mines in
1154 Saraburi Province, Thailand, 2021.
- 1155 Meier, S., Koene, E. F. M., Krol, M., Brunner, D., Damm, A., and Kuhlmann, G.: A lightweight NO₂-to-NO_x conversion model
1156 for quantifying NO_x emissions of point sources from NO₂ satellite observations, Atmospheric Chemistry and Physics, 24,
1157 7667–7686, <https://doi.org/10.5194/acp-24-7667-2024>, 2024.



- 1158 Miyazaki, K., Eskes, H., Sudo, K., Boersma, K. F., Bowman, K., and Kanaya, Y.: Decadal changes in global surface NO_x
1159 emissions from multi-constituent satellite data assimilation, *Atmospheric Chemistry and Physics*, 17, 807–837,
1160 <https://doi.org/10.5194/acp-17-807-2017>, 2017.
- 1161 Miyazaki, K., Sekiya, T., Fu, D., Bowman, K. W., Kulawik, S. S., Sudo, K., Walker, T., Kanaya, Y., Takigawa, M., Ogochi,
1162 K., Eskes, H., Boersma, K. F., Thompson, A. M., Gaubert, B., Barre, J., and Emmons, L. K.: Balance of Emission and
1163 Dynamical Controls on Ozone During the Korea-United States Air Quality Campaign From Multiconstituent Satellite Data
1164 Assimilation, *Journal of Geophysical Research: Atmospheres*, 124, 387–413, <https://doi.org/10.1029/2018JD028912>, 2019.
- 1165 Miyazaki, K., Bowman, K., Sekiya, T., Eskes, H., Boersma, F., Worden, H., Livesey, N., Payne, V. H., Sudo, K., Kanaya, Y.,
1166 Takigawa, M., and Ogochi, K.: Updated tropospheric chemistry reanalysis and emission estimates, TCR-2, for 2005–2018,
1167 *Earth System Science Data*, 12, 2223–2259, <https://doi.org/10.5194/essd-12-2223-2020>, 2020.
- 1168 Mues, A., Kuenen, J., Hendriks, C., Manders, A., Segers, A., Scholz, Y., Hueglin, C., Builtjes, P., and Schaap, M.: Sensitivity
1169 of air pollution simulations with LOTOS-EUROS to the temporal distribution of anthropogenic emissions, *Atmospheric
1170 Chemistry and Physics*, 14, 939–955, <https://doi.org/10.5194/acp-14-939-2014>, 2014.
- 1171 Nocedal, J. and Wright, S. J.: *Numerical optimization*, 2nd ed., Springer, New York, 664 pp., 2006.
- 1172 Oda, T., Maksyutov, S., and Andres, R. J.: The Open-source Data Inventory for Anthropogenic CO₂, version 2016
1173 (ODIAC2016): a global monthly fossil fuel CO₂ gridded emissions data product for tracer transport simulations and surface
1174 flux inversions, *Earth Syst. Sci. Data*, 10, 87–107, <https://doi.org/10.5194/essd-10-87-2018>, 2018.
- 1175 Park, J., Choi, Y., Jung, J., Lee, K., and Yeganeh, A. K.: First top-down diurnal adjustment to NO_x emissions inventory in
1176 Asia informed by the Geostationary Environment Monitoring Spectrometer (GEMS) tropospheric NO₂ columns, *Sci Rep*, 14,
1177 24338, <https://doi.org/10.1038/s41598-024-76223-1>, 2024.
- 1178 Park, J., Hong, H., Lee, H., Kim, S.-W., Kim, J., Van Roozendaal, M., Fayt, C., Ahn, M.-H., Jacob, D. J., Seo, S., Kim, K.-
1179 M., Kim, D., Choi, W., Lee, W.-J., Lee, D.-W., Wagner, T., Richter, A., Krotkov, N. A., Lamsal, L. N., Ko, D. H., Lee, S. H.,
1180 and Woo, J.-H.: Tropospheric nitrogen dioxide levels vary diurnally in Asian cities, *Commun Earth Environ*, 6, 389,
1181 <https://doi.org/10.1038/s43247-025-02272-7>, 2025.
- 1182 Park, R. J., Oak, Y. J., Emmons, L. K., Kim, C.-H., Pfister, G. G., Carmichael, G. R., Saide, P. E., Cho, S.-Y., Kim, S., Woo,
1183 J.-H., Crawford, J. H., Gaubert, B., Lee, H.-J., Park, S.-Y., Jo, Y.-J., Gao, M., Tang, B., Stanier, C. O., Shin, S. S., Park, H.
1184 Y., Bae, C., and Kim, E.: Multi-model intercomparisons of air quality simulations for the KORUS-AQ campaign, *Elementa:
1185 Science of the Anthropocene*, 9, 00139, <https://doi.org/10.1525/elementa.2021.00139>, 2021.



- 1186 Pörtner, H.-O., Roberts, D. C., Tignor, M. M. B., Poloczanska, E. S., Mintenbeck, K., Alegria, A., Craig, M., Langsdorf, S.,
1187 Löschke, S., Möller, V., Okem, A., and Rama, B. (Eds.): Climate Change 2022: Impacts, Adaptation and Vulnerability.
1188 Contribution of Working Group II to the Sixth Assessment Report of the Intergovernmental Panel on Climate Change., 2022.
- 1189 Rey-Pommier, A., Héraud, A., Chevallier, F., Ciais, P., Christoudias, T., Kushta, J., and Sciare, J.: Global gridded NO_x
1190 emissions using TROPOMI observations, *Earth System Science Data*, 17, 3329–3351, [https://doi.org/10.5194/essd-17-3329-](https://doi.org/10.5194/essd-17-3329-2025)
1191 2025, 2025.
- 1192 Ridley, B. A. and Grahek, F. E.: A Small, Low Flow, High Sensitivity Reaction Vessel for NO Chemiluminescence Detectors,
1193 1990.
- 1194 Ridley, B. A., Grahek, F. E., and Walega, J. G.: A Small High-Sensitivity, Medium-Response Ozone Detector Suitable for
1195 Measurements from Light Aircraft, 1992.
- 1196 Saide, P. E., Gao, M., Lu, Z., Goldberg, D. L., Streets, D. G., Woo, J.-H., Beyersdorf, A., Corr, C. A., Thornhill, K. L.,
1197 Anderson, B., Hair, J. W., Nehrir, A. R., Diskin, G. S., Jimenez, J. L., Nault, B. A., Campuzano-Jost, P., Dibb, J., Heim, E.,
1198 Lamb, K. D., Schwarz, J. P., Perring, A. E., Kim, J., Choi, M., Holben, B., Pfister, G., Hodzic, A., Carmichael, G. R., Emmons,
1199 L., and Crawford, J. H.: Understanding and improving model representation of aerosol optical properties for a Chinese haze
1200 event measured during KORUS-AQ, *Atmospheric Chemistry and Physics*, 20, 6455–6478, [https://doi.org/10.5194/acp-20-](https://doi.org/10.5194/acp-20-6455-2020)
1201 6455-2020, 2020.
- 1202 Santaren, D., Hakkarainen, J., Kuhlmann, G., Koene, E., Chevallier, F., Ialongo, I., Lindqvist, H., Nurmela, J., Tamminen, J.,
1203 Amorós, L., Brunner, D., and Broquet, G.: Benchmarking data-driven inversion methods for the estimation of local CO₂
1204 emissions from synthetic satellite images of XCO₂ and NO₂, *Atmospheric Measurement Techniques*, 18, 211–239,
1205 <https://doi.org/10.5194/amt-18-211-2025>, 2025.
- 1206 Seinfeld and Pandis: *Atmospheric Chemistry and Physics: From Air Pollution to Climate Change*, 3rd Edition | Wiley, 2016.
- 1207 Shetty, S. S., D, D., S, H., Sonkusare, S., Naik, P. B., N, S. K., and Madhyastha, H.: Environmental pollutants and their effects
1208 on human health, *Heliyon*, 9, <https://doi.org/10.1016/j.heliyon.2023.e19496>, 2023.
- 1209 Sicard, P., Agathokleous, E., Anenberg, S. C., De Marco, A., Paoletti, E., and Calatayud, V.: Trends in urban air pollution
1210 over the last two decades: A global perspective, *Science of The Total Environment*, 858, 160064,
1211 <https://doi.org/10.1016/j.scitotenv.2022.160064>, 2023.



- 1212 Skamarock, W. C., Klemp, J. B., Dudhia, J., Gill, D. O., Liu, Z., Berner, J., Wang, W., Powers, J. G., Duda, M. G., Barker, D.
1213 M., and Huang, X.-Y.: A Description of the Advanced Research WRF Model Version 4, <https://doi.org/10.5065/1DFH-6P97>,
1214 2019.
- 1215 Smith, S. J., van Aardenne, J., Klimont, Z., Andres, R. J., Volke, A., and Delgado Arias, S.: Anthropogenic sulfur dioxide
1216 emissions: 1850–2005, *Atmospheric Chemistry and Physics*, 11, 1101–1116, <https://doi.org/10.5194/acp-11-1101-2011>, 2011.
- 1217 St. Clair, J. M., Swanson, A. K., Bailey, S. A., and Hanisco, T. F.: CAFE: a new, improved nonresonant laser-induced
1218 fluorescence instrument for airborne in situ measurement of formaldehyde, *Atmospheric Measurement Techniques*, 12, 4581–
1219 4590, <https://doi.org/10.5194/amt-12-4581-2019>, 2019.
- 1220 Thailand Office of the National Economic and Social Development Board, World Bank: Industrial Change in the Bangkok
1221 Urban Region, 2017.
- 1222 Tuccella, P., Curci, G., Grell, G. A., Visconti, G., Crumeyrolle, S., Schwarzenboeck, A., and Mensah, A. A.: A new chemistry
1223 option in WRF-Chem v. 3.4 for the simulation of direct and indirect aerosol effects using VBS: evaluation against IMPACT-
1224 EUCAARI data, *Geoscientific Model Development*, 8, 2749–2776, <https://doi.org/10.5194/gmd-8-2749-2015>, 2015.
- 1225 Uttamang, P., Aneja, V. P., and Hanna, A. F.: Assessment of gaseous criteria pollutants in the Bangkok Metropolitan Region,
1226 Thailand, *Atmospheric Chemistry and Physics*, 18, 12581–12593, <https://doi.org/10.5194/acp-18-12581-2018>, 2018.
- 1227 Uttamang, P., Campbell, P. C., Aneja, V. P., and Hanna, A. F.: A multi-scale model analysis of ozone formation in the Bangkok
1228 Metropolitan Region, Thailand, *Atmospheric Environment*, 229, 117433, <https://doi.org/10.1016/j.atmosenv.2020.117433>,
1229 2020.
- 1230 Uttamang, P., Choomanee, P., Phupijit, J., Bualert, S., and Thongyen, T.: Investigation of Secondary Organic Aerosol
1231 Formation during O₃ and PM_{2.5} Episodes in Bangkok, Thailand, *Atmosphere*, 14, 994,
1232 <https://doi.org/10.3390/atmos14060994>, 2023.
- 1233 Valin, L. C., Russell, A. R., Hudman, R. C., and Cohen, R. C.: Effects of model resolution on the interpretation of satellite
1234 NO₂ observations, *Atmospheric Chemistry and Physics*, 11, 11647–11655, <https://doi.org/10.5194/acp-11-11647-2011>, 2011.
- 1235 Verreyken, B. W. D., Harkins, C., Li, M., Angevine, W., Stockwell, C. E., Xu, L., Coggon, M., Gilman, J., Warneke, C.,
1236 Strobach, E., Brown, S., McCarty, B., Marchbanks, R., Baidar, S., Brewer, A., Pfannerstill, E. Y., Arata, C., Goldstein, A. H.,
1237 Brioude, J., and McDonald, B. C.: Top-Down Evaluation of Volatile Chemical Product Emissions Using a Lagrangian
1238 Framework, *Environ. Sci. Technol.*, 59, 7211–7221, <https://doi.org/10.1021/acs.est.4c10117>, 2025.



- 1239 Ye, J., Liu, L., Wang, Q., Hu, S., and Li, S.: A Novel Machine Learning Algorithm for Planetary Boundary Layer Height
1240 Estimation Using AERI Measurement Data, *IEEE Geoscience and Remote Sensing Letters*, 19,
1241 <https://doi.org/10.1109/lgrs.2021.3073048>, 2021.
- 1242 Yu, K. A., Li, M., Harkins, C., He, J., Zhu, Q., Verreyken, B., Schwantes, R. H., Cohen, R. C., McDonald, B. C., and Harley,
1243 R. A.: Improved Spatial Resolution in Modeling of Nitrogen Oxide Concentrations in the Los Angeles Basin, *Environ. Sci.*
1244 *Technol.*, 57, 20689–20698, <https://doi.org/10.1021/acs.est.3c06158>, 2023.
- 1245 Zhao, C., Liu, X., Leung, L. R., Johnson, B., McFarlane, S. A., Gustafson, W. I. J., Fast, J. D., and Easter, R.: The spatial
1246 distribution of mineral dust and its shortwave radiative forcing over North Africa: modeling sensitivities to dust emissions and
1247 aerosol size treatments, *Atmospheric Chemistry and Physics*, 10, 8821–8838, <https://doi.org/10.5194/acp-10-8821-2010>, 2010.
- 1248 Zoogman, P., Liu, X., Suleiman, R. M., Pennington, W. F., Flittner, D. E., Al-Saadi, J. A., Hilton, B. B., Nicks, D. K.,
1249 Newchurch, M. J., Carr, J. L., Janz, S. J., Andraschko, M. R., Arola, A., Baker, B. D., Canova, B. P., Chan Miller, C., Cohen,
1250 R. C., Davis, J. E., Dussault, M. E., Edwards, D. P., Fishman, J., Ghulam, A., González Abad, G., Grutter, M., Herman, J. R.,
1251 Houck, J., Jacob, D. J., Joiner, J., Kerridge, B. J., Kim, J., Krotkov, N. A., Lamsal, L., Li, C., Lindfors, A., Martin, R. V.,
1252 McElroy, C. T., McLinden, C., Natraj, V., Neil, D. O., Nowlan, C. R., O'Sullivan, E. J., Palmer, P. I., Pierce, R. B., Pippin, M.
1253 R., Saiz-Lopez, A., Spurr, R. J. D., Szykman, J. J., Torres, O., Veefkind, J. P., Veihelmann, B., Wang, H., Wang, J., and
1254 Chance, K.: Tropospheric emissions: Monitoring of pollution (TEMPO), *Journal of Quantitative Spectroscopy and Radiative*
1255 *Transfer*, 186, 17–39, <https://doi.org/10.1016/j.jqsrt.2016.05.008>, 2017.
- 1256
- 1257
- 1258
- 1259
- 1260